JOURNAL OF PROPULSION AND POWER
Vol. 25, No. 4, July–August 2009

In-Stream Hypermixer Fueling Pylons in Supersonic Flow

Jason C. Doster* and Paul I. King†
Air Force Institute of Technology, Wright–Patterson Air Force Base, Ohio 45433
Mark R. Gruber‡ and Campbell D. Carter‡
U.S. Air Force Research Laboratory, Wright–Patterson Air Force Base, Ohio 45433
Michael D. Ryan§
Universal Technology Corporation, Dayton, Ohio 45432
and
Kuang-Yu Hsu¶
Innovative Scientific Solutions, Inc., Dayton, Ohio 45440

DOI: 10.2514/1.40179

This paper presents results from both computational fluid dynamic and wind-tunnel experiments of in-stream fueling pylons injecting air, ethylene, and methane gas into Mach number 2.0 cold airflow. Three fuel-injection pylons studied include a basic pylon, a ramp pylon, and an alternating-wedge pylon. The latter two pylons introduce streamwise vorticity into the flow to increase mixing action. The computational fluid dynamic solution was accomplished using the commercial code FLUENT®. Three wind-tunnel experimental techniques were used: aerothermal probing, Raman spectroscopy, and nitric-oxide planar laser-induced fluorescence. Four measures reported include streamwise vorticity, total-pressure-loss, mixing efficiency, and flammable plume extent. The ramp and alternating-wedge pylons show decisive increases in mixing capability compared with the basic pylon for a finite distance downstream of the injector. The alternating-wedge pylon exhibits a measurable increase in total pressure loss compared with the basic pylon, and the ramp pylon exhibits a negligible increase in total pressure loss compared with the basic pylon. For comparison, the downstream mixing effectiveness of the three pylons is compared with the downstream mixing effectiveness of a transverse circular wall injector studied in past research. In addition, a qualitative comparison between the computational fluid dynamic and wind-tunnel experimental results is made.

Nomenclature

A_e	=	effective fuel-injector area, m^2
A_f	=	fuel-plume area within flammable limits, m^2
A_p	=	fuel-plume area, m^2
C_d	=	coefficient of drag
d_e	=	equivalent diameter
f	=	fuel/air mass ratio
k	=	Boltzmann's constant, J/K
M	=	Mach number
MW	=	molecular weight, kg/kmol
$\dot{m}$	=	mass flow, kg/s
n	=	number density, number/m^3
P	=	static pressure, N/m^2
P_T	=	total pressure, N/m^2
q	=	momentum flux ratio
R	=	universal gas constant, J/kmol · K
T	=	static temperature, K
u	=	streamwise velocity, m/s
α	=	fuel mass fraction
γ	=	specific heat ratio
η_m	=	mixing effectiveness
Λ	=	total pressure loss
ρ	=	density, kg/m^3
ϕ	=	equivalence ratio
Ω_x	=	mass averaged streamwise vorticity, s^{-1}
ω_x	=	streamwise vorticity, s^{-1}

Presented as Paper 4501 at the 44th AIAA/ASME/SAE/ASEE Joint Propulsion Conference, Hartford, CT, 20–23 July 2008; received 31 July 2008; revision received 19 February 2009; accepted for publication 9 March 2009.

*Ph.D. Graduate, Department of Aeronautics and Astronautics. Member AIAA.
†Professor, Department of Aeronautics and Astronautics. Senior Member AIAA.
‡Senior Aerospace Engineer, Thermal and Electrochemical Branch. Associate Fellow AIAA.
§Research Scientist. Member AIAA.
¶Senior Research Scientist. Senior Member AIAA.

I. Introduction

THE scalability of scramjet combustor cross sections from smaller to larger applications is a weakness of high-aspect-ratio combustor geometries. A low-aspect-ratio circular or elliptical combustor geometry is easier to scale and also provides other advantages, including reduced wall friction and structural pressure loading efficiency. More interest of late has been focused on scramjet concepts using such combustor cross sections [1–6]. An in-stream fueling pylon concept for low-aspect-ratio scramjet combustors is studied here.

Uniform fuel distribution and rapid fuel mixing are both required of a scramjet fuel-injection system. An in-stream fueling pylon can distribute fuel uniformly due to its intrusive nature, and rapid mixing can be achieved in different ways. Transverse fuel injection into a combustor airflow promotes rapid fuel/air mixing [7–9]. However, momentum from the fuel stream does not contribute to engine thrust in this case. Injecting fuel parallel to the combustor airflow augments engine thrust, but mixing is a concern [10]. To increase the mixing effectiveness of parallel injection, the introduction of streamwise vortices into the combustor flow has shown promise, leading to the concept of the hypermixer [11,12]. The two hypermixer geometries studied here are swept compression ramps and alternating wedges [13–21].

The hypermixer geometries are incorporated onto the trailing edge of the in-stream fueling pylons. The mixing effectiveness of the two hypermixer pylons are compared with each other and a baseline pylon configuration with no hypermixer geometry on the trailing edge. Total pressure losses are also of concern, and so the mixing

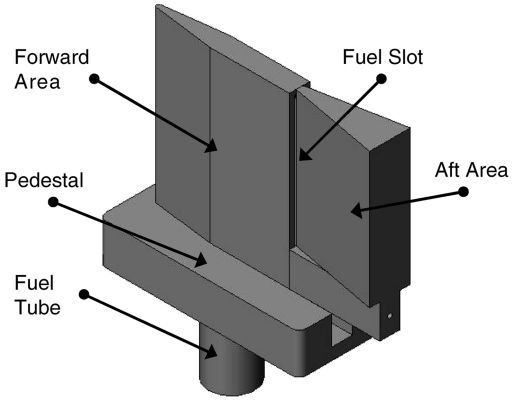

Fig. 1 Basic pylon configuration.

capability of each pylon is considered relative to its total pressure loss.

II. Pylon Configurations

Three pylon configurations include the basic pylon (Fig. 1), the ramp pylon (Fig. 2), and the alternating-wedge pylon (Fig. 3). Each pylon incorporates a two-piece forward and aft area. The forward area contains a plenum common to all pylons. The aft area forms a constant angled compression ramp on the basic pylon and a hypermixer geometry on the others. The mating of the two pieces creates thin rectangular injection slots. The common parameters for all pylons are height = 75 mm, length = 103 mm, frontal blockage area = 1215 mm^2, fuel port (slot) geometric area = 57 mm^2, front wedge half-angle = 14.7 deg, and front wedge nose radius = 1 mm.

The basic pylon embodies two fuel-injection strategies of 1) maximizing the fuel/air interface area with a rectangular slot and 2) injecting fuel upstream of the pylon aft area to allow fuel and air mixing before leaving the pylon surface. Figure 1 shows the basic pylon on a pedestal. The aft region of the basic pylon is a compression ramp at 10.6 deg (half-angle) to the main airflow. The plenum is fed by a fuel tube at the bottom of the pylon connected to the pedestal. Sonic fuel injection is accomplished from the slots, with a backward-facing step shielding the injectant for a short distance before mixing with the main airflow around the pylon.

The ramp pylon shown in Fig. 2 includes eight compression ramps on the aft area of the pylon. The compression ramps are 14.4 deg (half-angle) to the main airflow with 8.3 deg (half-angle) of ramp taper (sweep). The compression and sweep angles produce the same frontal blockage area as the basic pylon.

The alternating-wedge configuration shown in Fig. 3 includes eight alternating wedges on the aft area of the pylon. The wedge geometries have a 23.6 deg angle and attach to the aft area of the pylon, itself having a 14.4 deg compression angle (half-angle) to the main airflow. This configuration produces the same frontal blockage area as the other two pylons.

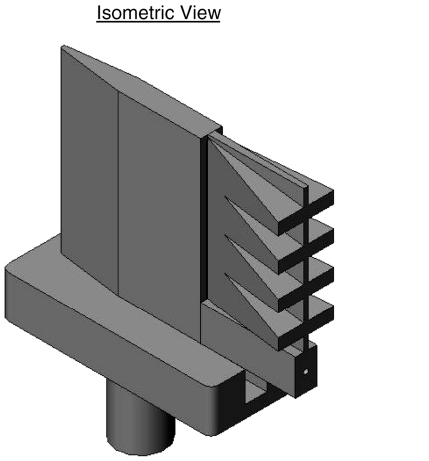

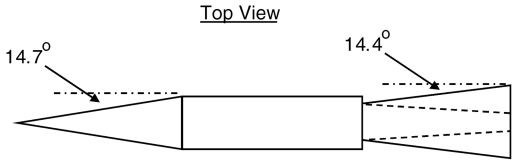

Fig. 2 Ramp pylon configuration.

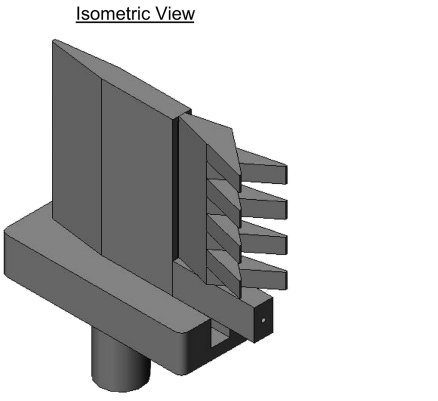

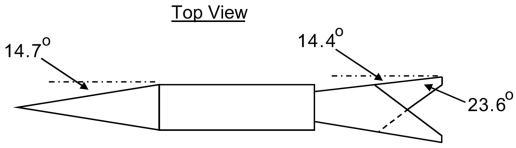

Fig. 3 Alternating-wedge pylon configuration.

III. Numerical Methodology

A. Grid Construction

A solid-body design for the three pylons was constructed in SolidWorks®. The solid-body design was output from SolidWorks and read into Gridgen® as an initial graphics exchange specification file in which surface domains were constructed and 2-D triangular meshes placed on the domains. These meshed surface domains were output from Gridgen and read into SolidMesh® as a Nastran® file, in which cells were constructed between the surface domains. Cells comprising the grids are an unstructured hybrid of tetrahedral/pentahedral cell volumes. The viscous tailoring of the grid near the pylon surfaces was accomplished to the refinement required to use the boundary-layer wall functions in FLUENT®.

The exterior walls of the computational domain are inviscid with slip flow for all three pylons, to limit grid size; hence, the grid is not refined with viscous spacing near the wind-tunnel walls. All pylon surfaces were defined with no-slip conditions as viscous boundaries. The wake region of all three pylons was populated with a dense cell mesh extending 290 mm downstream of the pylons. The cell volumes in the wake region are approximately 1 mm^3. The grids for the three pylons vary between 5.5–6.7 million cells. One grid was constructed for each pylon. Because of high grid cell density, a grid convergence study was not accomplished.

B. Flow Solution

FLUENT was the commercial computational fluid dynamics (CFD) code employed. A Reynolds-averaged Navier–Stokes second-order coupled solution for sonic ethylene injection from the pylon into a Mach number 2.0 wind-tunnel airflow was obtained for all three pylon configurations. Species transport with no combustion was modeled and the k-ω turbulence model with shear stress transport was used. Air/ethylene mixtures were assumed to act as an ideal gas, with physical properties of the mixture being an average within each computational cell, depending on the fractional species

makeup of the cell. Depending on the nature of the flow in the wake region of the pylons, the solution was progressed in a steady or an unsteady manner, using either a localized or global time step.

Solution convergence was determined three ways for a steady-state solution through 1) stability of the drag on the pylon; 2) reduction of the mass, velocity, and energy residuals at least 3 orders of magnitude from the original values; and 3) constant spatially integrated total mass flow and ethylene mass flow downstream of the pylons at each planar position sampled. The ramp and the alternating-wedge pylons have roughly steady flowfields in their wake regions and met all three convergence criteria through extended iterations of localized time-stepping. The basic pylon exhibits a highly unsteady flow and did not meet the mass flow requirement using localized time-stepping, and so a time-accurate solution was obtained for the basic pylon.

The freestream cold-airflow inlet and ethylene injection conditions are shown in Table 1. These conditions result in a unity momentum flux ratio q [Eq. (1)]:

$$q = \frac{(\gamma PM^2)_{\text{pylon}}}{(\gamma PM^2)_{\text{tunnel}}} = \frac{(\rho u^2)_{\text{pylon}}}{(\rho u^2)_{\text{tunnel}}} \tag{1}$$

C. Data Collection

The axial distance downstream of the injection slots is normalized by the equivalent diameter d_e, the diameter of a circle of equivalent geometric slot area (57 mm^2), 8.52 mm. The dense cell wake region extends 34 d_e downstream of the pylon base plane (aft rear face). The base plane of each pylon is 40 mm (4.7 d_e) aft of the injection slots. Figure 4 shows 14 downstream planar positions selected for reduction of four measures: streamwise vorticity, total pressure loss, mixing effectiveness, and flammable plume extent. These 14 positions correspond to 5.9 d_e, 7.4 d_e, 8.9 d_e, 10.6 d_e, 12.1 d_e, 13.6 d_e, 15.3 d_e, 16.8 d_e, 18.3 d_e, 20 d_e, 24.7 d_e, 29.4 d_e, 34 d_e, and 38.7 d_e aft of the injection slots.

1. Vorticity

Streamwise vorticity ω_x [Eq. (2)], is defined as the axial, or streamwise, component of the curl of the velocity vector. The mass averaged integral of the absolute value of axial vorticity is the measure of streamwise vorticity Ω_x [Eq. (3)]. Relative magnitudes of streamwise vorticity were computed, normalized by the maximum vorticity value present in the data globally at any planar position:

$$|\omega_x| = |(\nabla \times \boldsymbol{V})_x| \tag{2}$$

$$\Omega_x = \frac{\int |\omega_x| \rho u \mathrm{d}A}{\int \rho u \mathrm{d}A} \tag{3}$$

Total pressure loss Λ [Eq. (4)] was calculated from the mass averaged integral of total pressure [Eq. (5)]:

$$\Lambda = 1 - \frac{\bar{P}_T}{P_{T_{\text{tunnel}}}} \tag{4}$$

Table 1 Flow conditions for CFD simulation

Property/condition	Tunnel airflow	Pylon inj (ethylene)
Momentum flux ratio	——	1.0
Mass flux ratio	——	1.65
Mach number	2.0	1.0
Velocity	518 m/s	314 m/s
Mass flow	10.78 kg/s	0.04 kg/s
Total temperature	300 K	300 K
Static temperature	167 K	267 K
Total pressure	310 kPa	320 kPa
Static pressure	39.7 kPa	178 kPa
Geometric flow area	25, 161 mm^2	57 mm^2

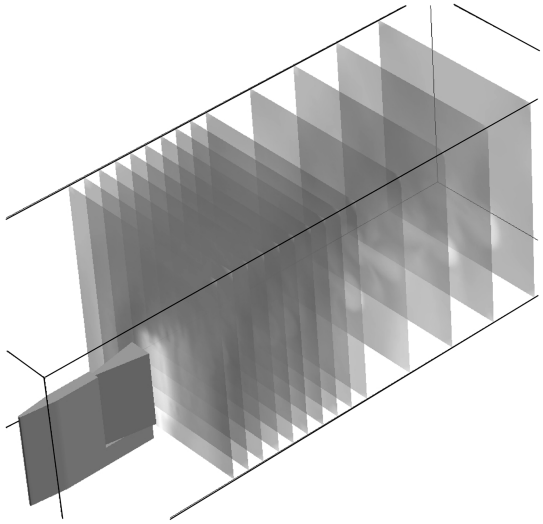

Fig. 4 Data-reduction planes.

$$\bar{P}_T = \frac{\int P_T \rho u \mathrm{d}A}{\int \rho u \mathrm{d}A} \tag{5}$$

2. Mixing

Mixing effectiveness η_m [Eq. (6)] is a measure of fuel dispersion (plume dilution) at a planar position [22,23]. Local (point) fuel mass fractions α [Eq. (7)] are obtained from simulation results. The stoichiometric mass fraction for a fuel/air mixture is calculated from Eq. (7) (f_s is the stoichiometric fuel/air mass ratio and ϕ is the equivalence ratio). For ethylene ($f_s = 0.068$), its mass fraction in air at stoichiometric conditions ($\phi = 1$) is $\alpha_s = 0.064$. The mixing-effectiveness calculation assumes that the least-available reactant, fuel or air, is the reactant considered for mixing. For instance, in a globally fuel-lean situation (which is the case here), the fuel is the mixing concern:

$$\eta_m = \frac{\dot{m}_{\text{fuel,mixed}}}{\dot{m}_{\text{fuel,total}}} = \frac{\int_{A_{\alpha=0}} \alpha_R \rho u \mathrm{d}A}{\int_{A_{\alpha=0}} \alpha \rho u \mathrm{d}A} \tag{6}$$

$$\alpha = \frac{\text{mass of fuel}}{\text{mass of fuel} + \text{mass of air}} = \frac{f}{f+1} = \frac{\phi f_s}{\phi f_s + 1} \tag{7}$$

$$\alpha_R = \begin{cases} \alpha, & \alpha \le \alpha_s \\ \alpha_s(1-\alpha)/(1-\alpha_s), & \alpha > \alpha_s \end{cases} \tag{8}$$

A local (point) value of mixing α_R, defined by Eq. (8), is evaluated from the local fuel mass fraction. At each point location, if the local fuel mass fraction is less than or equal to the mass fraction required for stoichiometric combustion, the fuel is fully mixed ($\alpha_R = \alpha$) there. If the local fuel mass fraction is greater than the stoichiometric mass fraction, the fuel is unmixed to some degree at that location, and α_R is reduced by a weighting function ($\alpha_R < \alpha$). The local mixing quantities are multiplied by the differential mass flow rate and integrated over the fuel-plume area in Eq. (6). The area of integration extends to the edges of the fuel plume in which the fuel mass fraction drops to zero or to some minimum detectable mass fraction (say, $\alpha \ge 0.001$). If the fuel plume is completely mixed at a planar location, the integrated mixing effectiveness $\eta_m = 1$. A fuel plume completely unmixed at a planar location has $\eta_m = 0$.

Mixing effectiveness does not tell the whole story. The amount of mixing is an indicator of how diluted the fuel is in the airstream, but there is a range of flammable mass fractions for a fuel/air mixture. If the plume mass fractions are too high, the mixture is too rich for

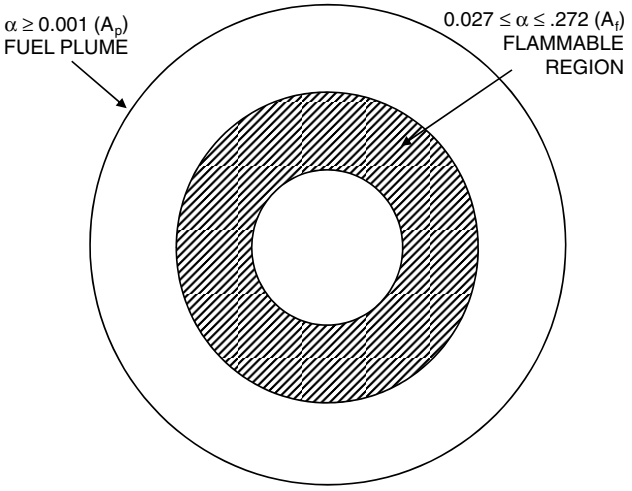

Fig. 5 Fuel plume.

combustion, and if the plume mass fractions are too low, the mixture is too lean. For a combustible mixture measure, one must evaluate the flammable plume extent.

Figure 5 illustrates a generic fuel plume. The shape (circular) is notional and not realistic. The flammable plume extent is characterized by two parameters [Eqs. (9) and (10)]. FP_a is the portion of fuel-plume area with fuel mass fractions falling within the flammable limits A_f, normalized by the effective fuel-injector area A_e. FP_f is A_f normalized by the fuel-plume area A_p. The first quantity compares the overall flammable plume area among pylons. The second determines the planar position in which the fuel plume exhibits the largest fraction of flammable area.

The flammability equivalence ratio limits for ethylene are $0.41 \leq \phi \leq 5.5$ [24]. Consequently, from Eq. (7), the range of flammable mass fractions of ethylene fuel in air is $0.027 \leq \alpha \leq 0.272$. The effective fuel-injector area A_e is $5.7E{-}5$ m^2 for CFD simulations, and the fuel-plume area A_p is the area of plume with ethylene mass fractions greater than 0.001:

$$\mathrm{FP}_a = \frac{A_f}{A_e} \tag{9}$$

$$\mathrm{FP}_f = \frac{A_f}{A_p} \tag{10}$$

IV. Experimental Methodology

Aerothermal probes, Raman spectroscopy, and planar laser-induced florescence (PLIF) were used to measure flow properties in the pylon wake region at multiple overlapping downstream planar positions during wind-tunnel experiments. All three experimental techniques have been implemented successfully in past research at the same test facility [8,9,25–27]. As with CFD, the downstream planar positions chosen for sampling are normalized by the geometric equivalent diameter d_e.

The nominal flow conditions for the wind-tunnel experiments are shown in Table 2. These nominal conditions are based on a momentum flux ratio equal to one between the pylon injection gas and the wind-tunnel airflow, just as in the CFD simulations. Note that the effective flow area in Table 2 for the pylons is not the geometric fuel port area (57 mm^2). It is the area calculated from mass flow calibration of the pylon. Boundary layers in the fuel port slots cause the effective fuel port area to be slightly smaller than the geometric area. This fueling slot area constriction was not taken into account in the CFD simulations.

$$q_m = \frac{(\rho u)_{\text{pylon}}}{(\rho u)_{\text{tunnel}}} \tag{11}$$

Different injectant gases will have different mass flux ratios [Eq. (11)] given the same momentum flux ratio. It is not possible to equate both the momentum flux ratio and the mass flux ratio between two experiments or simulations unless the molecular weight and total temperature of the injectant gases are the same. The CFD simulations used ethylene as the injectant gas, and the wind-tunnel experiments used air and methane as injectant gases. The momentum flux ratios between these different injectant gases and the airflow can be equated, but their mass flux ratios cannot. This results in different injectant-gas concentration values in the pylon wake region with each injectant gas.

A. Wind Tunnel

A continuous-flow supersonic wind tunnel was used for testing [28]. The wind tunnel produced the following conditions: Mach number of 1.95 and total pressure of 241 kPa (35 psi). The test section measured 132.1 mm (5.2 in.) high and 152.4 mm (6 in.) wide (slightly smaller than the CFD test section). The length of the test section was approximately 1 m. Optical windows (fused silica) were used for the test-section walls during laser experiments, and metal walls were used for aerothermal probe experiments. Below the test section was a three-axis movable table.

Injection gas for the pylon was supplied by high-pressure bottles stored outside the facility. The high-pressure gas was fed through a regulator that maintained the pressure entering the wind-tunnel room at approximately 1.38 MPa (200 psi). A Fairchild Industrial Products Company precision regulator (model 10264) reduced the pressure further to the pylon injection total pressures in Table 2. Total temperature and total pressure of the pylon injection gas were measured at the output end of the precision regulator just before entering the pylon plenum.

B. Aerothermal Probes

Three probes (thermocouple, cone static, and pitot) were used to measure total temperature, static pressure, and total pressure, respectively, in the wake region of the pylons at specific point locations. Three separate runs were required to obtain data with the three probes at the same locations. The cone static probe had a 10 deg half-angle cone tip with four small pressure ports at 90 deg intervals around the cone. The pitot probe tip outer and inner diameters were

Table 2 Nominal flow conditions for wind-tunnel experiments

Property/condition	Tunnel airflow	Pylon inj (air)	Pylon inj (methane)
Momentum flux ratio	——	1.0	1.0
Mass flux ratio	——	1.61	1.22
Mach number	1.95	1.0	1.0
Velocity	501 m/s	311 m/s	411 m/s
Mass flow	7.14 kg/s	0.031 kg/s	0.023 kg/s
Total temperature	288 K	288 K	288 K
Static temperature	164 K	240 K	249 K
Total pressure	241 kPa	240 kPa	249 kPa
Static pressure	33.3 kPa	127 kPa	135 kPa
Effective flow area	20, 129 mm^2	53.7 mm^2	53.7 mm^2

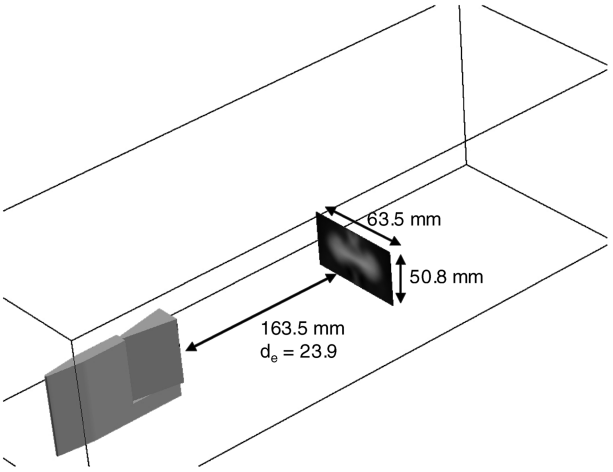

Fig. 6 Probing area.

3.175 mm (0.125 in.) and 1.588 mm (0.0625 in.), respectively. The thermocouple probe had the same outer and inner diameters as the pitot probe. The thermocouple probe tip was made of a ceramic material with two small holes in the side at 180 deg intervals for aspiration. A type-*K* small bead thermocouple was positioned just inside the ceramic tip shroud.

The wind-tunnel test section was configured with one metal sidewall and one window sidewall when aerothermal probes were used. The metal sidewall incorporated a slide that traversed in the vertical direction, driven by the movable table, to position the probe vertically inside the test section. A worm-gear traverser affixed to the movable table positioned the aerothermal probes horizontally.

A total of nine pylon air-injection experiments were accomplished to gather probe data on three pylon configurations at one planar position: 23.9 d_e. The probe response times were not fast enough to capture unsteady-flow phenomenon, and so averaged quantities were obtained. The data acquisition time for a single measurement was 0.5 s for the pressure probes and 1 s for the thermocouple probe. A two-dimensional grid of data was constructed at the same array of locations with each probe. Figure 6 illustrates the probing-area location. A 50.8 mm high by 63.5 mm wide (2 × 2.5 in.) array of 189 points was arranged with a 6.35 mm (0.25 in.) vertical spacing and 3.175 mm (0.125 in.) horizontal spacing. The bottom of the array was 12.7 mm (0.5 in.) above the wind-tunnel floor, and the middle of the array was centered on the wind-tunnel centerline.

Local Mach numbers, pressures, densities, and velocities were calculated from the three-probe data using a technique and program developed in past research [23]. The pylon wake flow at the plane of measurement was supersonic throughout. The data-reduction program incorporated the Rayleigh pitot equation to obtain local total pressure from pitot pressure, traversing the normal shock in front of the pitot probe. The exact numerical solution for a 10 deg cone in supersonic flow was used to obtain local static pressure from cone surface pressure, traversing the oblique shock in front of the cone probe. Isentropic relations were used to obtain all other local flowfield quantities. With the derived local Mach numbers, pressures, densities, and velocities from the three-probe data, Eq. (4) was again used to quantify the total pressure loss over the probing area.

C. Raman Spectroscopy

For the Raman experiments, the wind-tunnel test section was configured with two window sidewalls and a window top wall for optical access into the test section. Top- and side-view diagrams of the Raman setup are shown in Fig. 7. The light source was a Coherent, Inc., Verdi laser and a 4.5 W continuous source at 532 nm (green). The beam traversed through the test section at a single height above the floor and single planar position behind the pylon. The beam was focused to the center of the test section with a 1 m focal-length lens. To obtain a two-dimensional plume profile at a planar

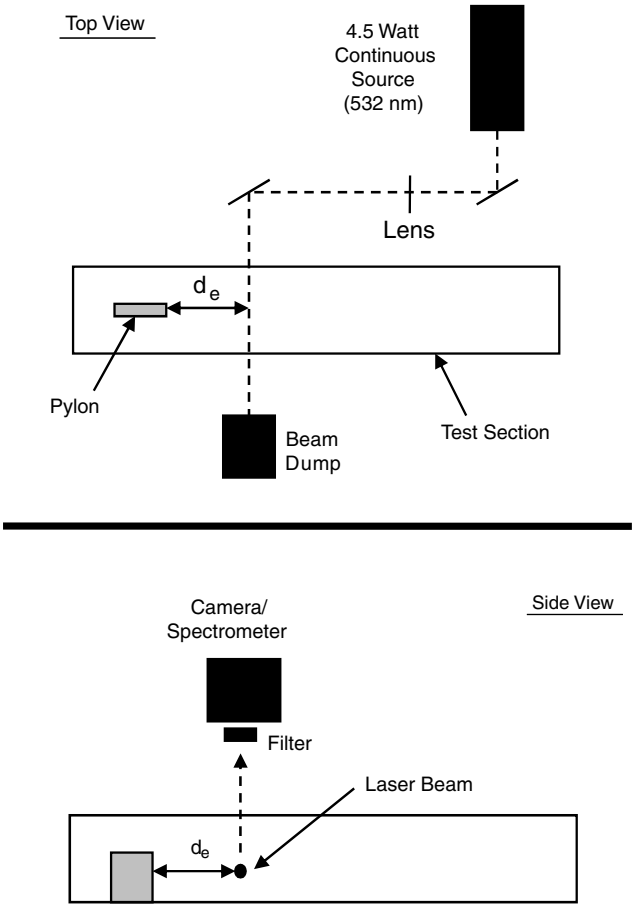

Fig. 7 Raman experiment setup.

position, the laser beam and imaging spectrometer were incrementally moved to multiple heights in a single test run using the movable table. The movable table also traversed the Raman setup to different planar positions between test runs.

Raman spectroscopy is a nonintrusive light interrogation technique used to sample concentrations of gases in the wind-tunnel flow by detecting molecular species of interest using inelastic light scattering [29,30]. The scattered light is shifted in frequency from the incident light by an amount that is dependent on the molecule, allowing detection and number density calculation of individual species in the mixture. With the incident 532 nm source, the shifted Stokes Raman signal for methane is at 634 nm, and the shifted signal for nitrogen is at 607 nm. Oxygen present in the wind-tunnel air also returns a Stokes Raman signal at 580 nm.

The camera/spectrometer equipment used to capture the Stokes Raman signal was a Kaiser Optical Systems, Inc., HoloSpec $f1.8$ aperture size, with an Andor Technology, plc, backilluminated charge-coupled device (CCD) detector. The imaging spectrometer was configured to record spectra over a range of approximately 550–650 nm. A mechanical shutter was used to control the exposure time of the imaging spectrometer. A Schott North America, Inc., glass long-pass filter (OG 570) was placed in front of the aperture to attenuate scattering at the laser source frequency (532 nm). The spectrometer also acted as a filter, because it was looking in the 550–650 nm frequency range. Filtering the light source frequency prevented Rayleigh and Mie scattering signals from overwhelming the Raman scattering signal.

Two calibration measurements were accomplished, both with no airflow in the wind tunnel and the test section loosely isolated from the rest of the wind tunnel by placing foam material upstream and downstream of the test section. The loose barriers were added to keep methane in the test section while calibration data were captured. The first measurement was taken with no methane present in the test section. Raman signals for oxygen and nitrogen were observed in this

calibration image. For the second measurement, methane was injected into the test section, and a few seconds were allowed for the methane to diffuse throughout before taking the measurement. Raman signals for oxygen, nitrogen, and methane were present in this calibration image. The two measurements are seen in Fig. 8. Each spectral calibration image is 128 pixels high and 256 pixels wide. Along with these two calibration image measurements, the temperature and pressure within the test section were recorded.

A total of six Raman experiments were accomplished to gather Raman signal data on three pylon configurations at two planar positions: 13.6 d_e and 23.9 d_e. At each planar position height, the camera shutter opened for 20 s to allow the Raman scattering signals time to integrate, then the movable table traversed the laser beam and imaging spectrometer to the next height. A two-dimensional grid of data 50.8 mm high by 63.5 mm wide (2 × 2.5 in.) was constructed. The bottom of the array was 12.7 mm (0.5 in.) above the wind-tunnel floor, and the middle of the array was centered on the wind-tunnel centerline. The vertical resolution was 3.175 mm (0.125 in.), and the horizontal resolution was approximately 0.254 mm (0.01 in.). During data reduction, the horizontal data were adjusted to 3.175 mm (0.125 in.) spacing so that the vertical and horizontal resolutions were comparable when constructing plume profiles.

An extensive data-reduction process was required to obtain methane mass fraction information from the Raman signal intensities. Two calibration curves relating Raman signal intensities to number densities of nitrogen and methane were required from the calibration process. The ratio of nitrogen to oxygen in air was assumed to not change with the amount of air present, and so the amount of nitrogen present was a direct measure of the amount of air present. Air and methane were both considered to be ideal gases under the range of pressures and temperatures experienced during testing. The total number density of molecules within the test section was a function of the temperature and pressure, seen in Eq. (12), where n is the number density and k is Boltzmann's constant:

$$P = nkT \tag{12}$$

The Raman signal intensity was assumed to vary linearly with concentration for both nitrogen and methane, due to the relatively small rovibrational excitation of the molecules. The number densities for each species were calculated through a set of simple simultaneous equations, knowing the total number density for each measurement from the test-section temperature and pressure and the signal intensities gathered from the spectral lines of each Raman calibration image. The simultaneous equations were solved for each vertical position in the calibration images, producing a calibration curve. The simultaneous equations are shown in Eqs. (13) and (14). Each vertical position horizontal slice is a horizontal position in the wind tunnel. A single horizontal slice from the spectral images of each calibration is seen in Fig. 9.

$$n_1 = c_1 I_{1_{N_2}} \tag{13}$$

$$n_2 = c_1 I_{2_{N_2}} + c_2 I_{2_{CH_4}} \tag{14}$$

where I_1 and I_2 are the Raman signal intensity values of each respective species from a horizontal slice. To calculate the I_1 and I_2 values of each species, the background signal (floor noise level) was subtracted from each horizontal slice and the top four intensity values averaged from the nitrogen and methane Raman signals. Solving for c_1 and c_2 at each vertical position yielded two calibration curves, shown in Fig. 10. The calibration is, to a good approximation, constant over a large extent of the horizontal viewing area, except at the left and right ends. This could be due to the camera/spectrometer pixel binning method, viewing path differences into the test section, or sensitivity differences near the edges of the CCD detector array. The reason for the behavior is not a concern, as long as it is accounted for in the calibration. The entire 128 pixel horizontal width of each Raman spectral data image was used to construct plume profiles.

The Raman spectral data image intensities were transformed into species number densities using the calibration curves. Each Raman spectral data image was the same size as the calibration images: 128 by 256. For a data image, the background signal was subtracted from each horizontal slice of the image, the top four intensity values for nitrogen and methane averaged, and the intensity values multiplied by their respective calibration curve values.

The final step was to calculate methane mass fractions from the nitrogen and methane number densities. The density of each species

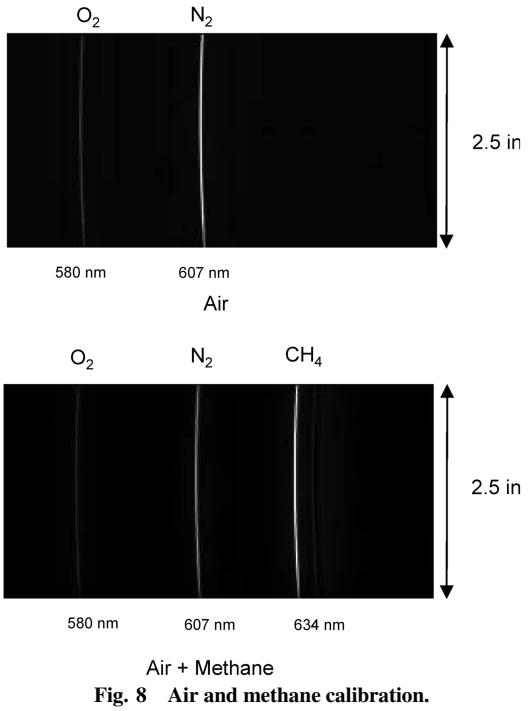

Fig. 8 Air and methane calibration.

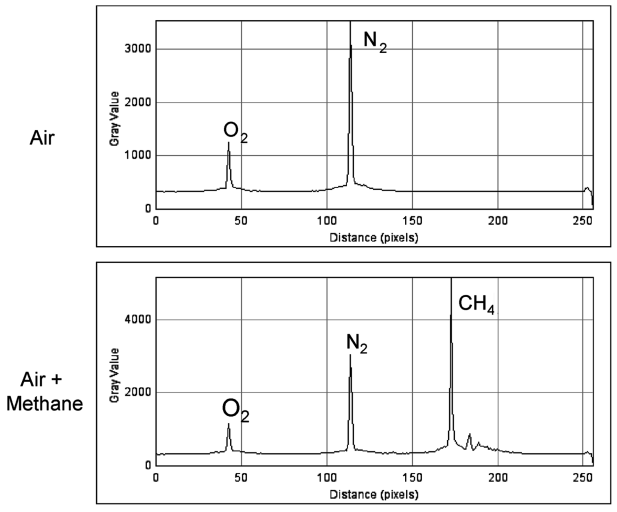

Fig. 9 Horizontal slices from Fig. 8.

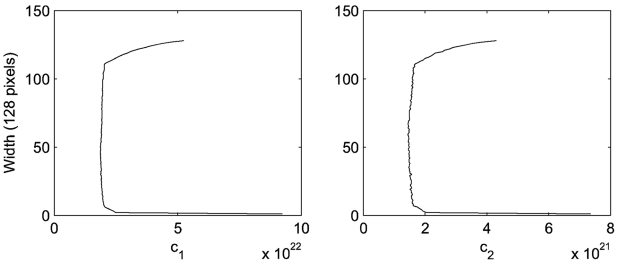

Fig. 10 Calibration curves for air and methane.

is a function of its number density multiplied by three constants [Eq. (15)]: Boltzmann's constant k, the species molecular weight (MW), and the universal gas constant R. The ratio of the methane density to air density is the methane/air mass ratio f, and the mass fraction of fuel in air α is defined by Eq. (7):

$$\rho = n\frac{k\mathrm{MW}}{R} \tag{15}$$

Methane mass fraction plume profiles were constructed at each planar position. The mixing effectiveness at a planar position is represented by the maximum methane mass fraction (maximum injectant concentration) in the fuel plume at that position. This is another type of plume-dilution measurement. There is not enough flowfield information available at each measurement location to accomplish the complicated mixing-efficiency calculation performed with the CFD simulation data, and so this mixing-effectiveness measure is a more simplistic approach. The maximum mass fraction decreases in the downstream direction as the methane is mixed into the airstream. A smaller maximum methane mass fraction indicates a more mixed fuel plume. The maximum mass fraction is calculated by taking the average of the top 1% of mass fraction values at a planar position to guard against a single data outlier.

The flammable plume extent measures [Eqs. (9) and (10)] were calculated using the methane mass fraction plume profiles just as they were calculated from CFD simulation data using ethylene mass fractions. However, a few changes were made to account for the injectant-gas difference. The flammability equivalence ratio limits for methane are $0.53 \leq \phi \leq 1.6$ [24]. The stoichiometric methane/air mass ratio f_s is approximately 0.058. Consequently, from Eq. (7), the range of flammable mass fractions of ethylene fuel in air is $0.030 \leq \alpha \leq 0.085$. The effective fuel-injector area A_e is $5.37E{-}5$ m^2, and the fuel-plume area A_p is the area of plume with fuel mass fractions greater than 0.001.

D. Planar Laser-Induced Fluorescence

Laser-induced fluorescence (LIF) is another nonintrusive light interrogation technique [29,30]. Fluorescence is the emission of radiation following deliberate resonant excitation of a molecule. A 1%-by-volume NO in N_2-seeding gas was added to pylon injection-air upstream of the pylon plenum (approximately 0.07% NO in air by mass). An electronic transition of the NO was stimulated using ultraviolet radiation distributed into a planar sheet (NO-PLIF). Top- and side-view diagrams of the NO-PLIF setup are shown in Fig. 11.

The radiation source was created through a combination of a Spectra-Physics, Inc., Quanta Ray Nd:YAG pulsed laser (GCR-170) and a Lumonics® hyperdye dye laser (HD-300). The second harmonic of the YAG laser (532 nm) pumped the dye laser, which produced 622 nm radiation. The 622 nm radiation was mixed with the third harmonic of the YAG (355 nm) using an Inrad Autotracker III system to produce approximately 226 nm radiation (ultraviolet). The pulse length was 10 ns and the pulse rate was 10 Hz rate. The power output was 5 mJ per pulse.

The laser setup was tunable and so a precise NO transition frequency could be identified. The NO transition used during experiments was $R_1(8.5)$ of the $A^2\Sigma^+ - X^2\Pi(0,0)$ band. The laser beam was distributed into a planar sheet using a planar concave cylindrical lens (−50 mm focal length) and a spherical convex lens (1 m focal length). The laser sheet was approximately 100 mm high, focused at the wind-tunnel test-section centerline.

The camera was a Roper Scientific, Inc., PI-MAX CCD with a Superblue intensifier and incorporated a Cerco® 45 mm $f/1.8$ UV lens. Unlike the Raman experiments, the camera viewed from a side angle and was attached to a Scheimpflug mount to mitigate image blur from the offnormal viewing angle. A 200 ns camera gate time was set to capture the fluorescence signals from the flowfield. A Schott UG-5 filter was placed in front of the camera lens to block scattering [as well as (0,0) fluorescence] at the frequency of the radiation source, passing fluorescence signals from the $(0,1), (0,2), (0,3), \ldots, (0,n)$ bands above 226 nm. The pulsed-laser setup was not fast enough for the camera to capture temporal flow changes with the fluorescence images. We obtained temporally resolved images that are uncorrelated (no relation between one another).

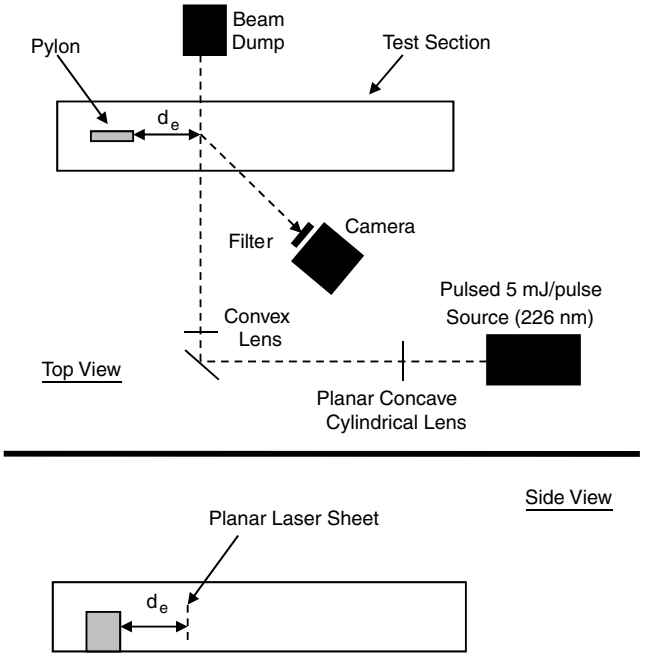

Fig. 11 NO-PLIF experiment setup.

The NO fluorescence signal was affected by differences in local flowfield temperatures and pressures due to electronic quenching and collisional line broadening. Pressure and temperature measurements were not taken in conjunction with the NO-PLIF measurements, and so no corrections were attempted. However, qualitatively, a change in NO-PLIF signal intensity can be interpreted as a monotonically similar change in NO concentration. This allows for a qualitative mixing (dilution) analysis of the pylon injectant plume based on NO-PLIF signal intensity values.

A total of 18 NO-PLIF experiments were accomplished to gather fluorescent signal data on three pylon configurations at six planar positions: 7.7 d_e, 10.7 d_e, 13.6 d_e, 16.6 d_e, 19.6 d_e, and 23.9 d_e. The third and sixth positions, 13.6 d_e and 23.9 d_e, were the same as the Raman experiments, and the sixth position was the same as the probe experiments. For each planar position, 300 images were collected over a 30 s period (10 Hz image rate).

In addition to data images, background and flat-field images were taken at each position. Flat-field images were taken under no-wind-tunnel-flow conditions with NO present in the test section. Background images were taken at each planar position under wind-tunnel flow but no NO seeding in the pylon injection air. The background images were used to remove background radiation from the data not associated with the LIF signals, and the flat-field images helped remove laser-sheet fluence and window transmission differences captured by the camera.

Before data reduction, each image was corrected for image perspective distortion (dewarped) due to the side viewing angle using a MATLAB® projective algorithm. Each image was 256×256 pixels before dewarping and 346×316 pixels after dewarping. The vertical and horizontal resolution of the dewarped images is approximately 0.254 mm/pixel (0.01 in/pixel). An example of a dewarped data image is shown in Fig. 12.

The first step in data reduction was to subtract the dewarped background images from the dewarped data images. The software used to manipulate the NO-PLIF data images was freeware called ImageJ. The average background image for each pylon and planar position was subtracted from the 300 dewarped data images for that same pylon and planar position. An example of a dewarped background image is shown in Fig. 13. The observable darker area in the middle is the result of the Mie scattering difference of the wind-

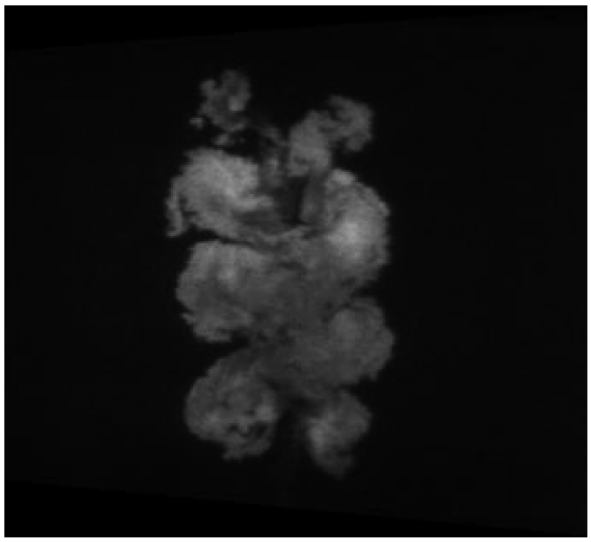

Fig. 12 Dewarped data image.

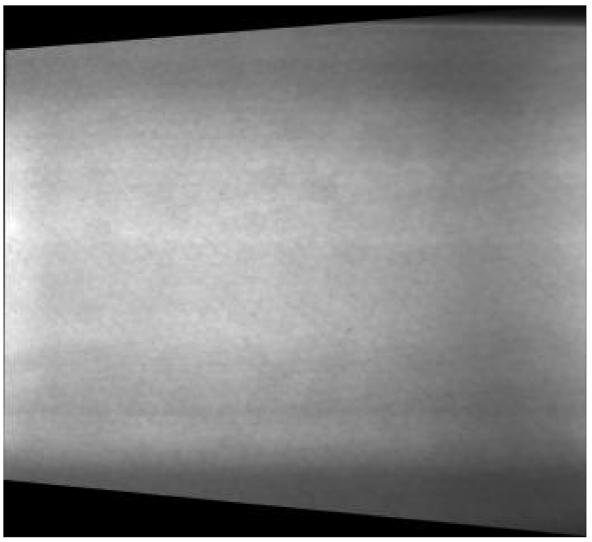

Fig. 14 Dewarped flat-field image.

tunnel air (moist) and the pylon injection air (dry) from the supply bottles outside the test facility.

The second step was to use the dewarped flat-field images to normalize the data images. The flat-field image for each pylon and planar position was normalized so that the average pixel intensity in the image was approximately 1.0 in magnitude. Then the normalized image was divided into the 300 background subtracted data images for that same pylon and planar position. An example of a dewarped flat-field image is shown in Fig. 14. The nonuniformity of the flat-field image due to laser-sheet fluence and window transmission differences is visually apparent, although a uniform concentration of NO is present in the test section.

The third step was to flip the data images horizontally (looking downstream instead of upstream) so they matched the probe and Raman experimental data profile orientations. The resultant 18 data image sets contained 300 instantaneous snapshots each, providing instantaneous spatial flowfield information. The images were cropped and read into MATLAB for further analysis. The final fluorescent images are 66.04 mm high by 76.2 mm wide (2.6×3 in.). The bottom of the images is 12.7 mm (0.5 in.) above the wind-tunnel floor, and the middle is centered on the wind-tunnel centerline.

MATLAB was used to plot fluorescent signal plume profiles next to each other, accomplish plume-dilution calculations, and observe the differences between average and instantaneous flowfield information. Plume-dilution measurements were accomplished the same way as in the Raman experiments. However, instead of mass fraction values, the top 1% of pixel intensity values within the images were averaged and compared among planar positions to observe how quickly the fuel plume mixed with the airstream.

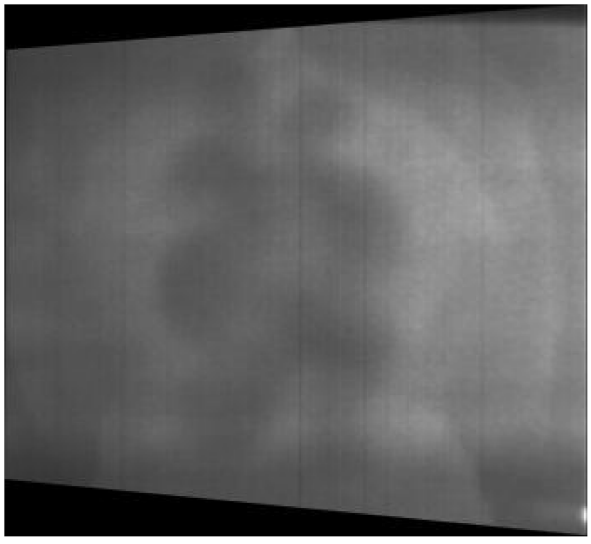

Fig. 13 Dewarped background image.

V. Numerical Simulation Results

The steady-state solution (localized time-stepping) attempted for the basic pylon exhibited highly unsteady flow in the form of vortex shedding. Although localized time-stepping resulted in reduced residuals about 3 orders of magnitude from original values and a steady drag on the pylon, the total mass flow downstream of the pylon was not constant; thus, a time-accurate solution was necessary for the basic pylon. The vortex shedding exhibited a frequency of 6900 Hz or a Strouhal number [Eq. (16)] of 0.24 ($V = 518$ m/s and $d = 0.018$ m):

$$St = \frac{fd}{V} \tag{16}$$

A time step of 1 ms was selected to resolve the shedding frequency. This time step results in about 145 iterations per one vortex-shedding period. The solution was advanced in time until a consistent periodic pattern emerged. The solution snapshot at the final time step was kept for analysis. The solution was then advanced one half-period further, and that solution snapshot was also kept for analysis. Data were collected at the 14 downstream planar positions in both instantaneous snapshots, one half-period separated in time. The four measures of streamwise vorticity, total pressure loss, mixing efficiency, and flammable plume extent were calculated in each snapshot and then averaged between the snapshots. As it turned out, all the measure values were virtually identical in the two time snapshots.

The ramp and alternating-wedge pylon solutions both exhibited a constant mass flow in their wake region and met the steady drag and residual reductions required for steady-state solution convergence using localized time-stepping. This is not to say the flow downstream of these pylons is perfectly steady, just steady enough to satisfy the convergence criteria selected for the simulations. From CFD solution attempts, it appears the streamwise vorticity production of the ramp and alternating-wedge pylons promotes a more steady flow in the wake region, because vortex shedding is not present in these solutions.

The mass flow in the wake region of the three pylons is compared in Fig. 15. For the two steady solutions, the total mass flow and ethylene mass flow are constant in the wake region. For the basic pylon time-accurate solution, the total mass flow and ethylene mass flow in the wake region vary slightly, but do not, on average, grow in

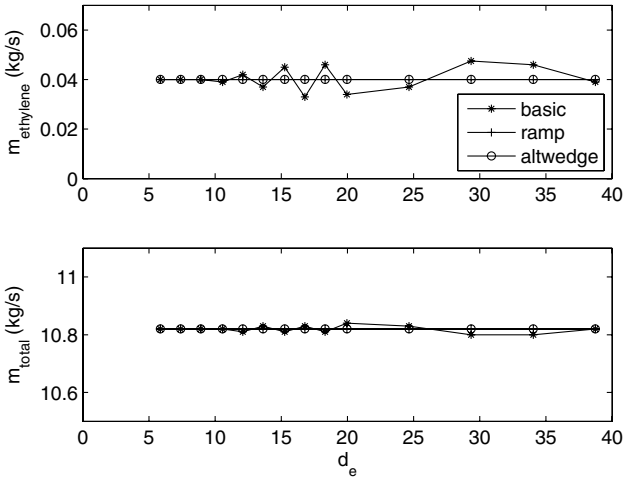

Fig. 15 Mass flow comparison.

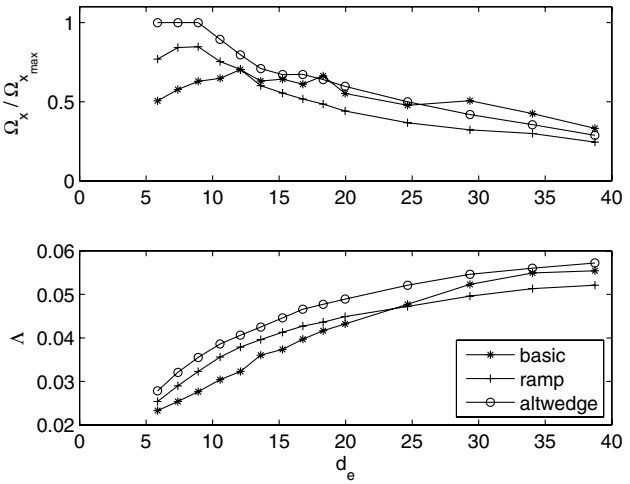

Fig. 16 Vorticity and pressure loss comparison.

deviation from the mean with downstream distance. The mass flow values oscillate around the correct values of 10.82 and 0.04 kg/s, respectively.

The streamwise vorticity and total pressure loss, computed from Eqs. (3) and (4), respectively, are compared in Fig. 16. It is difficult to make direct planar position comparisons between the basic pylon and the other two, given the slight mass flow variations in the basic pylon time-accurate solution. However, there are general trends. The streamwise vorticity immediately downstream of the ramp and alternating-wedge pylons is increased over the basic pylon due to the vortical inducing geometries at the aft end of those pylons. In this narrow region is the opportunity for the ramp and alternating-wedge pylons to mix fuel and air more rapidly than the basic pylon. Looking past the near field, the difference in streamwise vorticity among the pylons is much less.

The total pressure loss of the alternating-wedge pylons exceeds that of the basic and ramp pylons. The ramp pylon total pressure loss is greater than the basic pylon in the near field, but the total pressure loss of the basic pylon exceeds that of the ramp pylon as downstream distance increases into the far field.

The nondimensional drag due to surface pressures and viscosity is the drag coefficient, which is defined in Eq. (17). The dynamic pressure multiplied by the pylon frontal area is 134.9 N in the simulation cold flow for all pylons, because each has the same frontal area by design. The drag coefficients are presented in Table 3. The alternating wedge has the highest drag penalty, followed by the basic pylon and then the ramp pylon:

$$C_d = \frac{\text{drag}}{\frac{1}{2}\rho u^2(\text{area})} = \frac{\text{drag}}{134.9\ \text{N}} \tag{17}$$

Figure 17 shows the mixing efficiency of the pylons. In general, mixing efficiency increases with downstream distance. The alternating-wedge pylon exhibits the greatest mixing efficiency throughout the wake region.

Figure 18 shows the flammable plume extent. The alternating-wedge pylon has the largest flammable plume area FP_a throughout the wake region. The alternating-wedge and ramp pylons both show a maximum flammable plume fraction FP_f around 10 d_e, upstream of the basic pylon maximum flammable plume fraction around 20 d_e. Both hypermixer pylons have larger FP_f fractions of the fuel plume nearer the pylon base plane compared with the basic pylon.

Table 3 Pylon drag

Pylon	C_d	Drag, N
Basic	0.61	82
Ramp	0.59	80
Alternating wedge	0.66	89

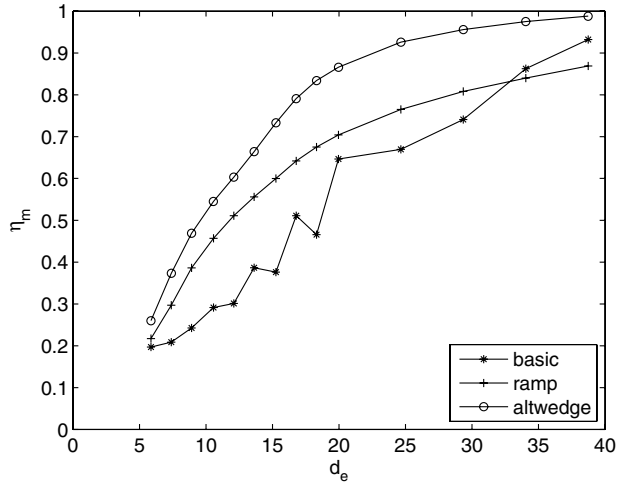

Fig. 17 Ethylene/air mixing comparison.

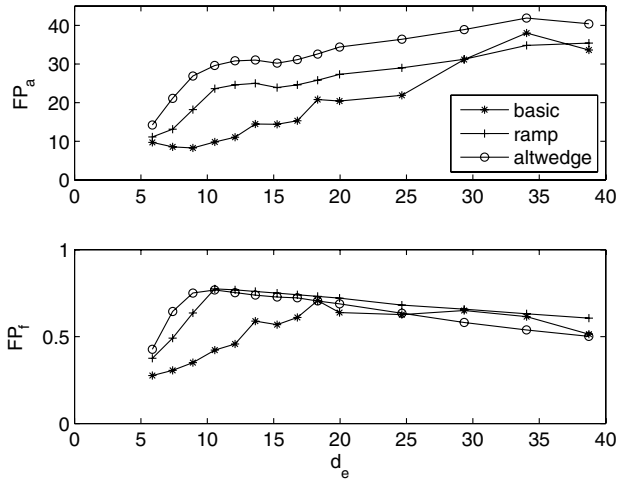

Fig. 18 Flammable plume comparison.

CFD simulations indicate that the alternating-wedge pylon offers the greatest mixing and flammable plume extent as well as the greatest total pressure loss and drag. The ramp pylon offers an increase in mixing and flammable plume extent over the basic pylon, with a negligible total pressure loss and drag change compared with the basic pylon. Between the two hypermixing pylons, the alternating-wedge offers better mixing and flammable plume extent

at the expense of higher total pressure loss and drag. With these overall trends from simulation in mind, the wind-tunnel experimental results are discussed in the next section.

VI. Experimental Results

A. Planar Laser-Induced Fluorescence

Figure 19 shows one instantaneous image out of the 300 for each pylon, along with the ensemble-averaged image of all 300 instantaneous images at 13.6 d_e. The basic pylon plume is highly unsteady, exhibiting side-to-side movement about the centerline of the plume (vortex shedding). An instantaneous image from the basic pylon varies substantially from the ensemble-averaged image. An instantaneous image from the ramp and alternating-wedge pylons also shows some variation from the ensemble-averaged image, but much less than the basic pylon. The wake-region flow of the two hypermixer pylons is much steadier than that of the basic pylon. These experimental results validate what was seen in CFD simulations. A steady-state solution was unable to be produced for the basic pylon, because the wake of that pylon is indeed quite unsteady.

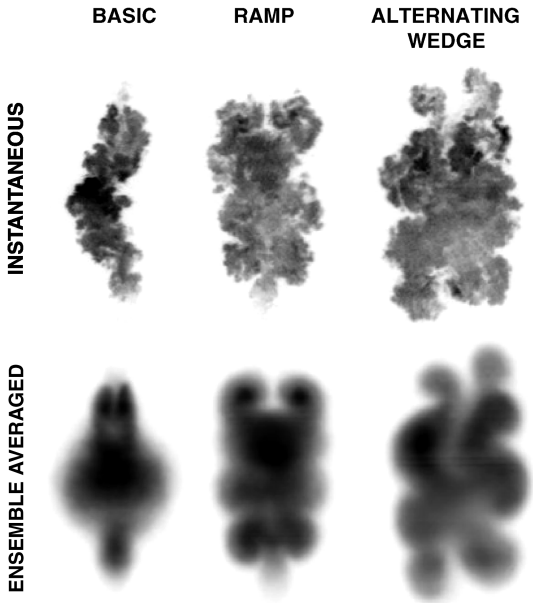

Fig. 19 NO-PLIF images at 13.6 d_e.

Figures 20 and 21 show ensemble-averaged plume-profile images of all three pylons at six planar positions. The pixel intensities of each image are normalized by the maximum pixel intensity present at each respective planar position. The darkest image at a planar position corresponds to the least mixed fuel plume, and the lightest image corresponds to the most well mixed. Because the fuel-plume intensity profiles are normalized by planar position, lightness/darkness comparisons between positions cannot be made with these plots. We attempted to globally normalize all fuel-plume intensity profiles, but the mixing rate behind the pylons was rapid enough that the pixel intensities at planar positions farther downstream were too white in the grayscale to be observed visually.

At the three planar positions closest to the pylon base in Fig. 20, the basic pylon has the darkest plume and is therefore the least mixed of the three. The ramp and alternating-wedge pylons are lighter and similar in contrast, indicating they have similar mixed states at these planar positions. At planar positions farther downstream in Fig. 21, there is less of a contrast difference between the three pylon plumes, indicating less of a mixed-state difference between the three. At the farthest planar position, 23.9 d_e, the basic and ramp pylons are similar in darkness, indicating that their mixed states are similar, whereas the alternating-wedge appears slightly lighter in contrast, indicating a more mixed state than the other two.

Plume shapes can be visually compared among planar positions in Figs. 20 and 21. The basic pylon plume close to the pylon base is a vertically long, thin strip of injectant gas. The plume spreads out horizontally and contracts in height as it grows in size with

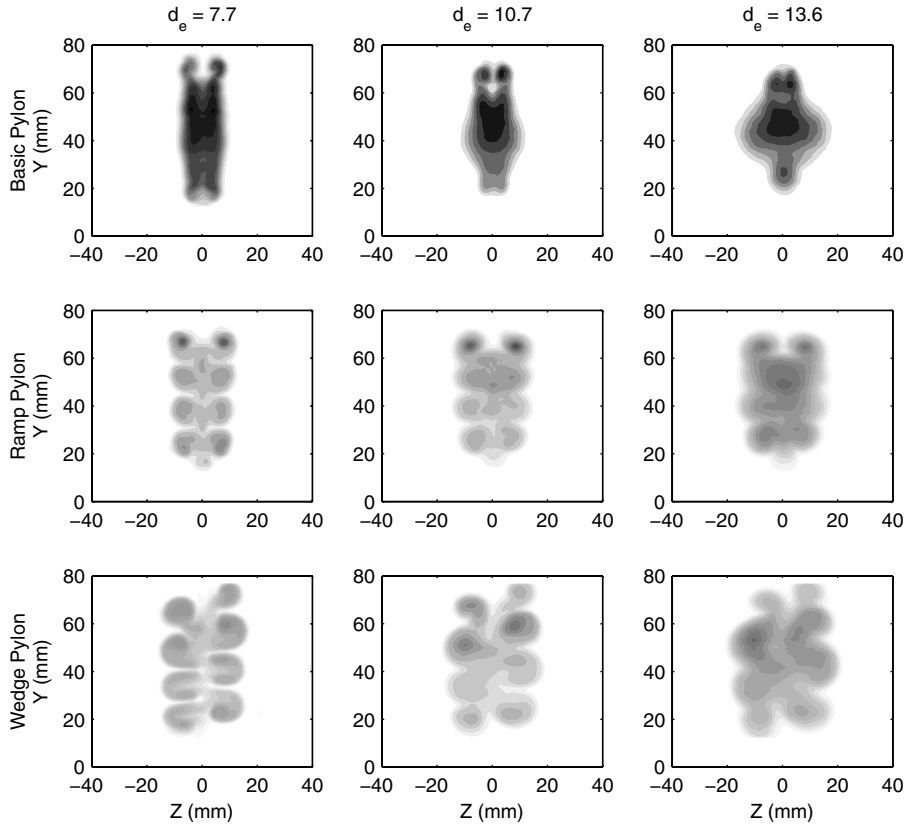

Fig. 20 NO-PLIF average plume-profiles for 7.7 d_e, 10.7 d_e, and 13.6 d_e.

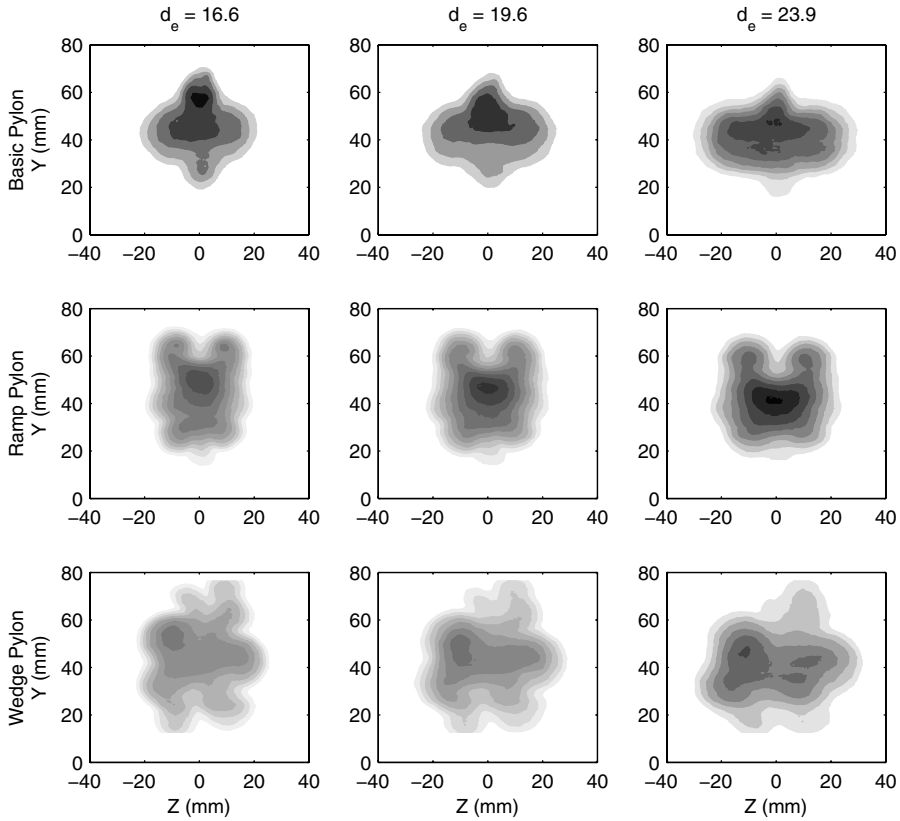

Fig. 21 NO-PLIF average plume profiles for 16.6 d_e, 19.6 d_e, and 23.9 d_e.

downstream distance. This vertical-to-horizontal plume shape change is called axis switching. The ramp pylon has tightly concentrated axial vortical structures close to the pylon base plane that help preserve the vertical extent of the ramp plume with downstream distance. The alternating-wedge pylon also has intense vortical structures close to the pylon base plane that help preserve the vertical extent of the alternating-wedge plume moving downstream. Axis switching is not observed as much in the downstream development of the hypermixer pylons. The axis switching of the basic pylon is mostly a result of the ensemble averaging. The basic pylon instantaneous plume images are shifting left and right across the centerline of the plume due to the vortex shedding. The horizontal extent of the ensemble-averaged plume image for the basic pylon is the mean horizontal variation over time. The plume is not actually present in the full horizontal extent at any one instant.

A comparison of maximum pixel intensity values among planar positions is shown in Fig. 22. They represent the relative level of mixing at each planar position, although qualitative in nature due to the experimental technique. The maximum pixel intensity values in each plume profile are normalized by the maximum pixel intensity globally. The maximum pixel intensity globally is located in the 7.7 d_e planar intensity profile of the basic pylon. Because all maximum pixel intensities are normalized across planar positions, comparisons among positions can be made using Fig. 22.

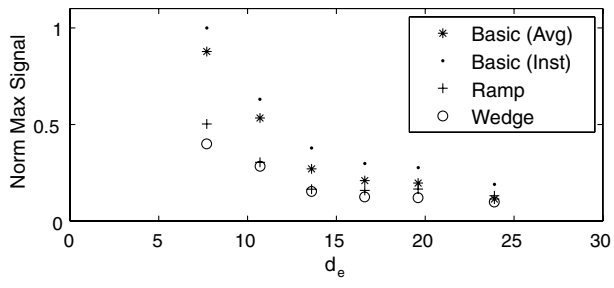

Fig. 22 NO-PLIF normalized maximum pixel intensity comparison.

The maximum pixel intensity trends for the pylons match the visual observations of the plume intensity profiles in Figs. 20 and 21. The ramp and alternating-wedge pylons mix the injectant into the wind-tunnel flow more quickly in the near field, resulting in lower maximum pixel intensities compared with the basic pylon. However, the basic pylon eventually matches the mixing capability of the hypermixers further downstream. The ramp and alternating-wedge pylons are very close in their maximum pixel intensities at every planar position, but the alternating-wedge does show a slight mixing advantage at most positions.

A distinction should be made between ensemble-averaged and instantaneous pixel intensity values. The ensemble-averaged values overestimate the mixed state of the fuel plume compared with the instantaneous values. Figure 22 displays the basic pylon maximum pixel intensities for both the ensemble-averaged values and the instantaneous values. The maximum pixel intensities are calculated differently in each case. The maximum pixel intensities for the ensemble-averaged profile are calculated by averaging the top 1% of pixel intensities in the ensemble-averaged plume profiles. The maximum pixel intensities for the instantaneous profiles are calculated by averaging the top 1% of pixel intensities in each of the 300 instantaneous images for each planar position, then averaging the 300 maximum intensity values to obtain a representative maximum pixel intensity for each position.

If the fuel plumes were perfectly steady, the calculations should be the same. One is the maximum of the instantaneous plume pixel intensities averaged, and the other is the maximum of the averaged plume pixel intensities. However, in an unsteady flow, the calculations produce different results. To illustrate the difference, Fig. 23 shows the maximum pixel intensities using the ensemble-averaged and instantaneous information for the three pylons at the six planar positions.

It is important to understand whether there is statistical significance between the maximum pixel intensities (the top 1% sample averages). This is determined using the standard deviation of each sample. The averaged maximum pixel intensities are statistically different at the 90% confidence level if they are separated by

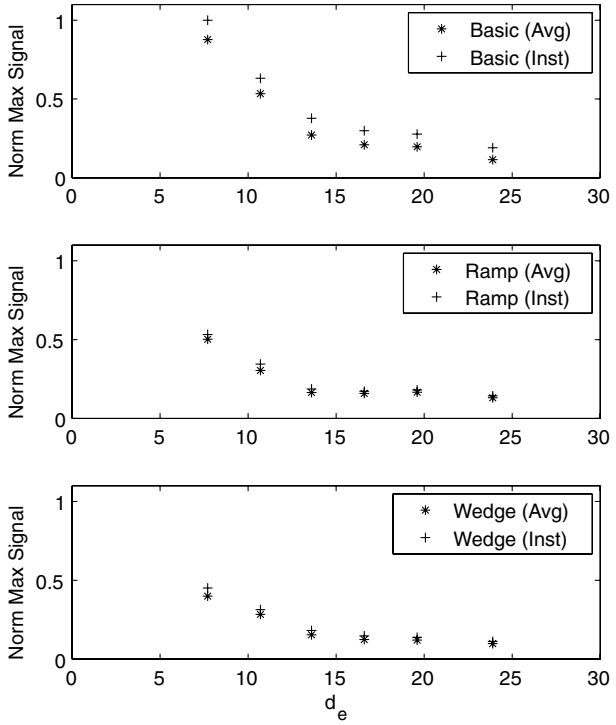

Fig. 23 NO-PLIF average versus instantaneous image maximum pixel intensities.

more than their standard deviations summed and multiplied by 1.282 [31]. The normalized average and standard deviation values for each sample are shown in Table 4, and Table 5 shows whether the maximum plume pixel intensity values are statistically different at the 90% confidence level (Y denotes yes and N denotes no).

The basic pylon instantaneous and averaged maximum pixel intensity values are statistically different at the 90% confidence level at all planar positions. The instantaneous values are consistently higher than the averaged values. The ramp and alternating-wedge pylon instantaneous and averaged values are not statistically different from one another at all planar positions, and the ramp and alternating-wedge pylons show much less difference overall between instantaneous and averaged maximum pixel intensity values, compared with the basic pylon.

Spatially averaging unsteady-flow quantities tends to depress peaks in the data. Because the basic pylon has more unsteadiness in its wake region compared with the hypermixer pylons, the ensemble-averaged images depress the maximum pixel intensities to a greater extent. This results in an overestimation of the mixing capability if using the ensemble-averaged values rather than the instantaneous values. The hypermixer pylons show much less of a difference between the average and instantaneous values.

The logical question to ask is whether the instantaneous information or the ensemble-averaged information is more indicative of the plume's susceptibility to combustion over time. That question cannot be answered by these experiments. Combustion experiments are required. However, the authors believe that the instantaneous composition of fuel and air mixtures is a better indication of combustion potential than the ensemble-averaged composition of fuel and air, because the instantaneous flowfield is where the fuel and air are actually meeting. It is important to note that the Raman experiments gathered average plume information due to the long integration time of the Raman signal. Mass fraction values from those experiments more than likely overestimate the basic pylon mixing capability and, to a much lesser extent, the hypermixer pylons.

B. Raman Spectroscopy

Mass fraction profiles constructed using Raman data at 13.6 d_e and 23.9 d_e are shown, along with ensemble-averaged NO-PLIF plume profiles, in Figs. 24 and 25. The plume shapes obtained with each experimental technique are quite similar, almost identical. A visual comparison can be made between the Raman mass fraction profiles in each figure. Lower mass fractions indicate a better mixed, and therefore more diluted, fuel plume. The Raman mass fractions are reduced at 23.9 d_e compared with 13.6 d_e. This is to be expected, because the former is farther downstream and has more time to mix with the airstream. At 13.6 d_e, the ramp and alternating-wedge pylons result in noticeably lower mass fractions than the basic pylon, with the alternating-wedge having the lowest mass fractions. At 23.9 d_e, the alternating-wedge pylon is still the most diluted of the three, and the ramp and basic pylons exhibit about the same dilution. This is the same trend observed in the NO-PLIF plume profiles at 13.6 d_e and 23.9 d_e. The ramp and alternating-wedge pylons mix the injectant and airstream in a shorter distance, but the basic pylon eventually achieves a level of mixing similar to the hypermixer pylons as downstream distance increases.

Table 4 NO-PLIF-averaged versus instantaneous maximum pixel intensity values

Pylon	Statistic	7.7 d_e	10.7 d_e	13.6 d_e	16.6 d_e	19.6 d_e	23.9 d_e
Basic (inst)	Mean	1.0000	0.6312	0.3776	0.2981	0.2767	0.1902
	Sdev	0.0546	0.0284	0.0181	0.0144	0.0132	0.0091
Basic (avg)	Mean	0.8776	0.5335	0.2706	0.2095	0.1965	0.1142
	Sdev	0.0133	0.0040	0.0032	0.0047	0.0037	0.0012
Ramp (inst)	Mean	0.5327	0.3441	0.1867	0.1720	0.1805	0.1428
	Sdev	0.0575	0.0394	0.0092	0.0057	0.0055	0.0045
Ramp (avg)	Mean	0.5025	0.3038	0.1647	0.1586	0.1658	0.1310
	Sdev	0.0572	0.0345	0.0029	0.0025	0.0017	0.0017
Wedge (inst)	Mean	0.4505	0.3134	0.1811	0.1467	0.1376	0.1119
	Sdev	0.0281	0.0180	0.0098	0.0065	0.0048	0.0037
Wedge (avg)	Mean	0.3996	0.2840	0.1537	0.1240	0.1208	0.0980
	Sdev	0.0121	0.0129	0.0062	0.0029	0.0017	0.0014

Table 5 NO-PLIF-averaged versus instantaneous maximum pixel intensity statistical difference

Comparison	7.7 d_e	10.7 d_e	13.6 d_e	16.6 d_e	19.6 d_e	23.9 d_e
Basic (inst)/basic (avg)	Y	Y	Y	Y	Y	Y
Ramp (inst)/ramp (avg)	N	N	Y	Y	Y	Y
Wedge (inst)/wedge (avg)	N	N	Y	Y	Y	Y

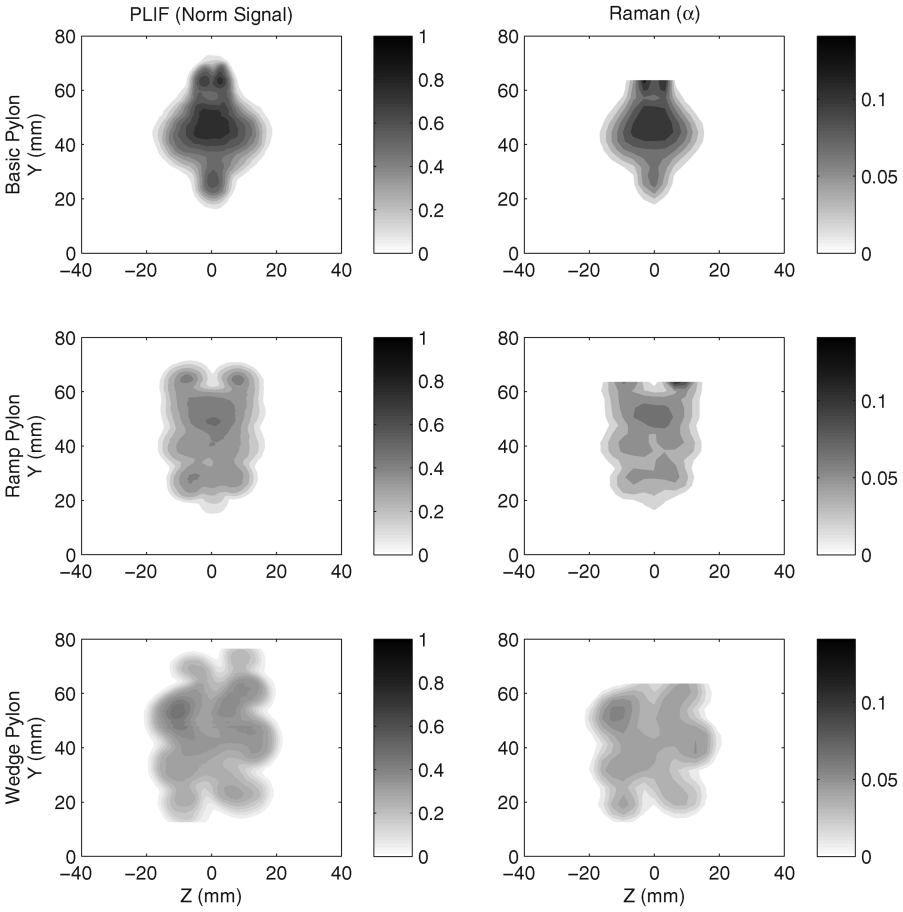

Fig. 24 Raman and NO-PLIF profile comparison at 13.6 d_e.

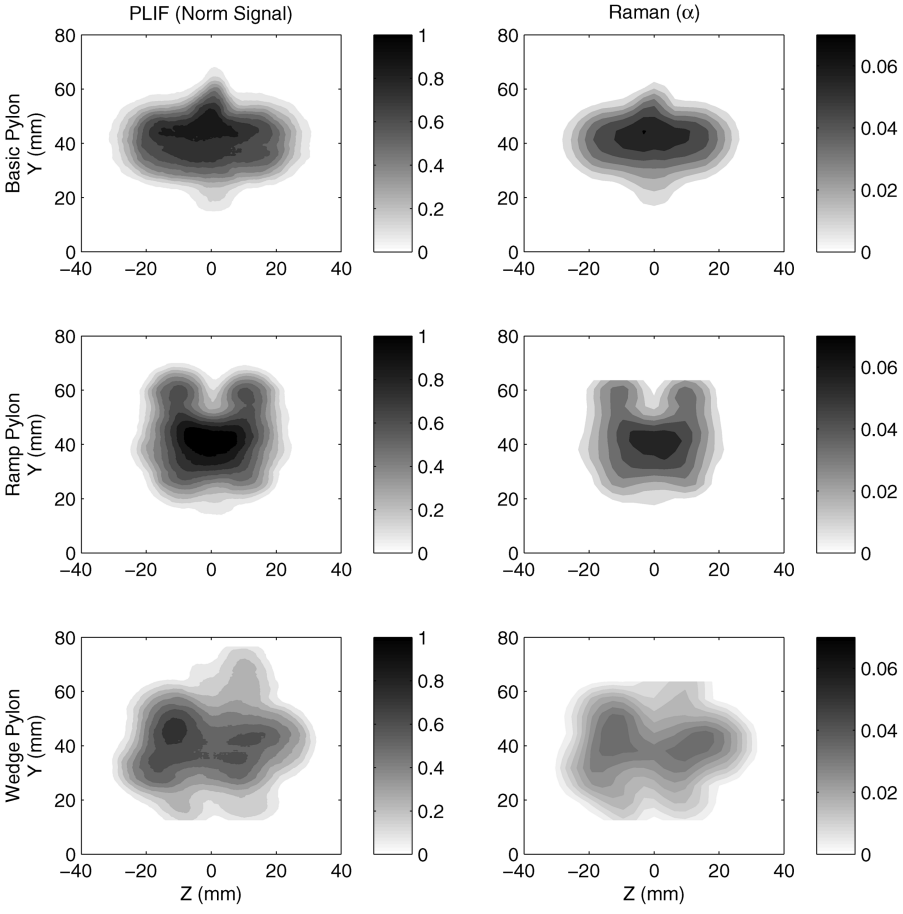

Fig. 25 Raman and NO-PLIF profile comparison at 23.9 d_e.

The maximum methane mass fraction at each planer position for each pylon is shown in Fig. 26. Lower maximum methane mass fractions indicate a better mixed fuel plume. The quantitative comparison supports the visual comparisons. The plumes of all three pylons become better mixed progressing downstream. At 13.6 d_e the hypermixer pylons have a more well mixed plume than the basic pylon. At 23.9 d_e there is less overall mixing difference between the pylon plumes, but the alternating-wedge pylon is slightly more mixed than the other two. These results support the NO-PLIF results. The streamwise vortex production associated with the hypermixer pylons aids mixing in the near field, but becomes less effective in the far-field region.

Figure 27 shows the flammable plume areas and flammable plume fractions for each mass fraction profile. The largest flammable plume area and highest flammable plume fraction are found in the alternating-wedge pylon case at 13.6 d_e. At this planar position, about 65% of the methane/air mixture is combustible. At this same planar position, the ramp pylon has the second-largest flammable plume area/fraction, almost matching the alternating-wedge pylon, and the basic pylon has the smallest flammable plume area/fraction. About 25% of the basic pylon plume is flammable at 13.6 d_e.

The story is much different at 23.9 d_e. The flammable plume measures from the three pylons are much closer. The alternating-wedge has the smallest flammable plume area/fraction, the ramp pylon has the largest, and the basic pylon is very close to the ramp pylon. The methane/air mixture behind the alternating-wedge pylon at this planar position has been diluted so much that many of the local mass fractions have fallen below flammability limits. The ramp pylon's flammable plume fraction has also fallen off at this planar position, but not as much as the alternating-wedge pylon. The basic pylon's flammable plume area/fraction has increased at 23.9 d_e from 13.6 d_e, because many of the local mass fractions above the flammability limit closer to the pylon base plane fall into the flammable region farther away.

These measures verify that the hypermixer pylons reduce downstream mixing distance compared with the basic pylon. Between the ramp and alternating-wedge pylons, the alternating wedge creates a larger flammable plume and reaches a slightly higher flammable plume fraction. The mixing differences between the two hypermixer pylons are much less pronounced than the differences between the hypermixer pylons and the basic pylon.

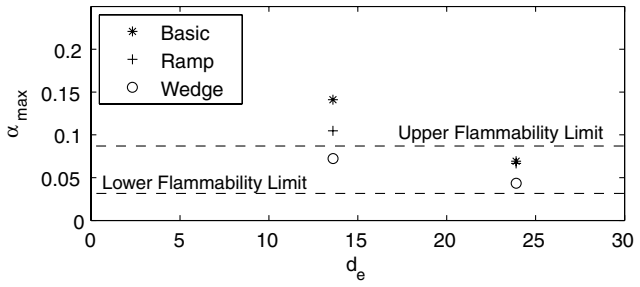

Fig. 26 Raman maximum mass fraction values.

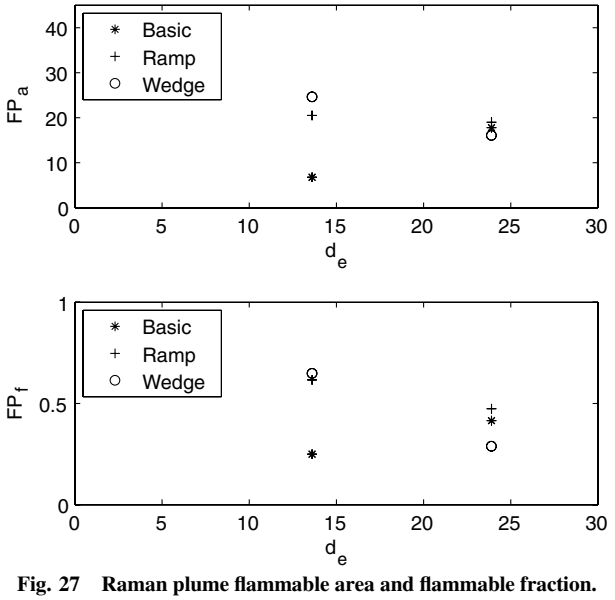

Fig. 27 Raman plume flammable area and flammable fraction.

C. Experimental Technique Comparison

The Raman and NO-PLIF experiments measured injectant concentrations and constructed wake-region plume profiles. The injectant gases in each case were different. The Raman experiments used methane and the NO-PLIF experiments used air. The momentum flux ratios were kept the same in both cases, but due to the injectant-gas differences, the mass flux ratios were different. Therefore, the amount of mass flow from the pylons in each experiment was slightly different. Data from the Raman experiments were in the form of mass fractions, and data from the NO-PLIF experiments were in the form of signal intensities. There were two positions at which both Raman and NO-PLIF measurements were collected: 13.6 d_e and 23.9 d_e.

There is a large resolution difference between the Raman and NO-PLIF plume profiles. The NO-PLIF signal intensity values have an order-of-magnitude-better resolution than the Raman mass fraction values, and so the edges of the fuel plumes are resolved more finely. Also, in the vertical direction, the Raman data were only collected up to 63.5 mm (2.5 in.) above the wind-tunnel floor, whereas the NO-PLIF data were collected up to 78.7 mm (3.1 in.) above the wind-tunnel floor. More of the fuel-plume vertical extent was captured in the NO-PLIF data.

The plume shapes and signal intensity distributions are very similar using both experimental techniques. In the Experimental Methodology section, it was argued that although NO-PLIF data were qualitative, the fluorescence signal could be considered to monotonically increase with increasing pylon injectant concentrations. This allowed a general plume mixing comparison between the pylons using NO-PLIF signal intensity values. Figures 24 and 25 both visually appear to support this monotonic relationship. In addition, a quantitative fuel-plume location-by-location comparison between Raman mass fraction values and NO-PLIF signal intensity values is done to show this relationship. Raman mass fraction values are calibrated and are used as a relative truth source to compare against the NO-PLIF intensity values in this analysis, but due to mass flux differences, the comparison cannot be used as a concentration calibration for the NO-PLIF intensity values.

The NO-PLIF intensity values are sampled at the resolution of the Raman methane mass fraction array for this comparison, and the fuel-plume comparison region extends to edges of the Raman fuel plume. Figure 28 plots the Raman-calculated methane mass fraction against the NO-PLIF signal intensity for all locations inside the fuel-plume comparison region at planar positions 13.6 d_e and 23.9 d_e. A monotonic (generally linear) relationship between pylon injectant concentration and NO-PLIF signal intensity is observed. There is scatter in the data due to the qualitative nature of the NO-PLIF measurements, but the trend is apparent. More scatter is present at 13.6 d_e than at 23.9 d_e. This is expected, because pressure and temperature variations are larger at planar positions closer to the base plane of the pylon.

D. Total Pressure Loss

Total-pressure-loss data were calculated using the aerothermal probes with air injection from the pylons. The first column of Table 6 shows total-pressure-loss data using the aerothermal probes. The basic pylon results in the least total pressure loss, and the alternating-wedge pylon has the most, at 23.9 d_e. Compared with the basic pylon, the ramp pylon total pressure loss is 9% greater and the alternating-wedge total pylon pressure loss is 33% greater.

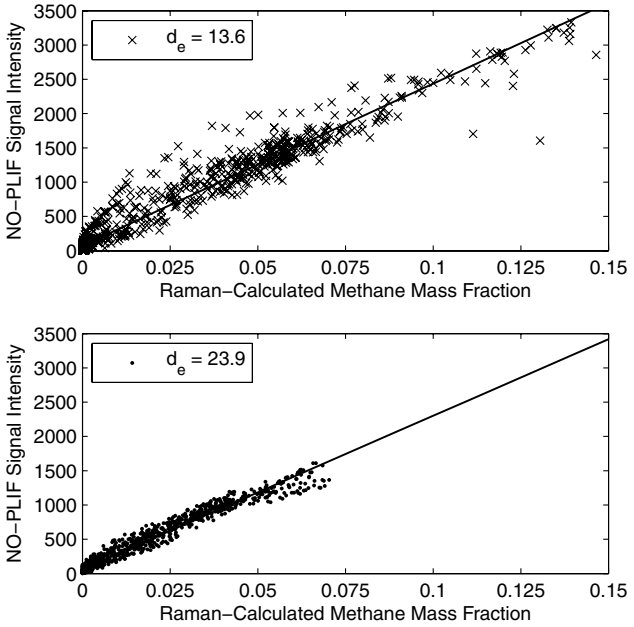

Fig. 28 NO-PLIF signal intensity comparison with Raman concentration.

To compare total pressure loss between simulation and experiment, the simulation total pressure losses had to be recalculated. The aerothermal probes only sampled the pylon wake region over a small area (50.8 mm high by 63.5 mm wide), and so simulation total pressure loss was recalculated using flow quantities from this identical area. In addition, aerothermal probe flow quantities were temporally averaged due to the acquisition time of the probes. The instantaneous CFD flow quantities were ensemble-averaged over one vortex-shedding period to account for this averaging.

The second column of Table 6 shows the recalculated total pressure loss for the CFD simulations at 23.9 d_e. The experimental aerothermal probe total-pressure-loss measurements support the CFD simulation total-pressure-loss trends among the pylon configurations. Even though the numerical total-pressure-loss values from CFD and aerothermal probe data are not very close due to test-condition differences between simulation and experiment, the trends between the pylons are striking similar.

The ramp and basic pylons both have very similar total pressure losses at 23.9 d_e in simulation and experiment. In the case of the aerothermal probes, the difference is a little greater than in simulation, but in both cases, the total pressure loss of the basic and ramp pylons are close. The alternating-wedge pylon consistently shows a greater total pressure loss than the basic and ramp pylons at 23.9 d_e in simulation and experiment. The same trend is seen throughout the pylon wake region in simulation results (Fig. 16). The alternating-wedge has a larger total pressure loss compared with the basic and ramp pylons, and the basic and ramp pylons are more similar in their total pressure loss.

VII. Mixing Comparisons Between Simulation and Experiment

There were slight test-condition differences in Mach and Reynolds numbers between the CFD simulations and the wind-tunnel experiments. In addition, injectant concentration measurements between simulations and experiments varied due to injectant-gas

Table 6 Total-pressure-loss comparison at 23.9 d_e

Pylon	Λ (probes)	Λ (CFD)
Basic	0.184	0.243
Ramp	0.200	0.244
Alternating wedge	0.244	0.288

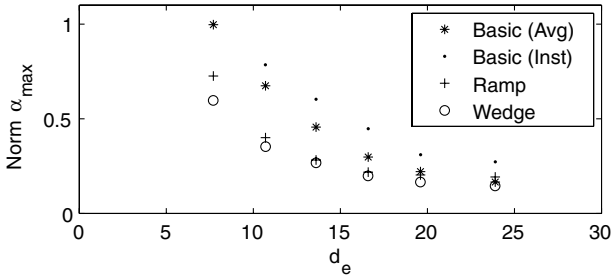

Fig. 29 CFD-normalized maximum ethylene mass fraction comparison.

(mass flux) differences. The Raman experiments used methane injection, the NO-PLIF and aerothermal probe experiments used air injection, and the CFD simulations used ethylene injection from the pylon. In all cases, the momentum ratios of the injectant gases to wind-tunnel airflow were kept the same, but the mass flux ratios varied, depending on injectant gas. The mass flux ratio of methane injection varied more than 25% from air or ethylene injection, resulting in plume-profile concentration differences at the same planar positions.

Although these differences exist between the simulation and experiment, a purely qualitative comparison in mixing measures is possible. The NO-PLIF experiments injected air seeded with a small amount NO. The CFD simulations incorporated ethylene injection. Ethylene and air have very similar molecular weights and therefore have very similar mass flux ratios. A plume-dilution comparison at six planar positions can be done between simulation and experiment.

Figure 29 shows a plume-dilution comparison among pylon configurations using CFD maximum ethylene mass fraction values. The maximum ethylene mass fraction values are shown at the same planar positions as the NO-PLIF maximum pixel intensities in Fig. 22. The maximum ethylene mass fraction values are all normalized by the maximum global ethylene mass fraction at any planar position (at 7.7 d_e in the basic pylon instantaneous image). The nonnormalized average and standard deviation values for each maximum ethylene mass fraction sample are shown in Table 7.

The maximum ethylene mass fraction values in Fig. 29 from the CFD simulation exhibits the same qualitative trend among the pylon configurations as the maximum plume pixel intensity values in Fig. 22 from the NO-PLIF measurements. The hypermixer pylons mix the injectant more quickly than the basic pylon, but the difference in mixing capabilities lessens with downstream distance. The ensemble-averaged ethylene mass fraction values overestimate the mixing capability of the basic pylon compared with the instantaneous values. The ramp and alternating-wedge pylons are very close in their mixing ability, but the alternating-wedge plume is mixed slightly better at most planar positions.

A second comparison can be made between ethylene mass fraction data from simulations accomplished here and experimental data from a single-hole transverse wall injector studied in past research [9,32]. The past experimental data come from plane wall transverse ethylene injection into a Mach number 2.0 airflow with a momentum ratio of 1.0, the same equivalency parameters used in simulations accomplished here.

The plume-dilution measurement used in the past research is the ethylene/air maximum equivalence ratio $\phi_{\max}$. The past research states that the downstream decay rate of the maximum equivalence ratio of a single transverse injection hole at a momentum ratio of one is a power-law function defined by Eq. (18). A plume-dilution measurement used in CFD simulation accomplished here is the maximum ethylene mass fraction $\alpha_{\max}$. A conversion between maximum ethylene mass fraction and maximum ethylene/air equivalence ratio is shown in Eq. (19). This equation is derived from Eq. (7), and $f_s = 0.068$ for an ethylene/air mixture:

$$\phi_{\max} = 21.7 d_e^{-0.78} \tag{18}$$

Table 7 CFD maximum ethylene mass fraction values

Pylon	Statistic	7.7 d_e	10.7 d_e	13.6 d_e	16.6 d_e	19.6 d_e	23.9 d_e
Basic (inst)	Mean	0.6315	0.4958	0.3810	0.2828	0.1958	0.1723
	Sdev	0.0076	0.0221	0.0299	0.0230	0.0152	0.0084
Basic (avg)	Mean	0.6297	0.4258	0.2879	0.1882	0.1396	0.1045
	Sdev	0.0072	0.0234	0.0098	0.0040	0.0036	0.0034
Ramp (avg)	Mean	0.4587	0.2530	0.1748	0.1378	0.1284	0.1217
	Sdev	0.0209	0.0070	0.0052	0.0014	0.0027	0.0012
Wedge (avg)	Mean	0.3766	0.2234	0.1693	0.1256	0.1041	0.0921
	Sdev	0.0289	0.0143	0.0073	0.0049	0.0037	0.0014

$$\phi_{\max} = \frac{\alpha_{\max}}{f_s(1-\alpha_{\max})} \tag{19}$$

Figure 30 shows an ethylene plume-dilution comparison between the single-hole transverse wall injector and in-stream pylon injectors moving downstream. The spatial comparison is from the point at which the ethylene is injected. For the single-hole transverse injector, this is from the center of the hole. For the pylons, this is 4.7 d_e upstream of the base plane of the pylon, where the fueling slots are located.

The plume-dilution data in Fig. 30 show that the hypermixer pylon injectors equal the mixed state of the transverse injector around 10–15 d_e. Upstream of this planar position, the single-hole transverse injection does a better job of mixing the ethylene and air, and downstream of this planar position, the hypermixer pylons equal or better the transverse injector. This is a promising result. The hypermixer geometries were placed on the parallel injection pylons to better their mixing capability, because pure parallel injection does not mix as well as transverse injection. The ethylene/air mixture behind the hypermixer pylons matches that from a single transverse injection hole in a short distance behind the pylon base plane.

If the location of comparison between the two injectors was different [say, the hole location (transverse injector) and the pylon base plane (pylon injector)], the pylon mixing would fare much better in the comparison. All the pylon plume-dilution data would shift 4.7 d_e to the left, and the alternating-wedge pylon would equal the mixing effectiveness of the transverse hold injector at all planar positions. However, in fairness to the transverse hole injector, the location of ethylene injection is the most logical place to compare the two injectors.

VIII. Conclusions

Three pylon configurations are compared in their performance as in-stream fuel injectors for use in a scramjet combustor supersonic flow. The first pylon is a baseline, and the other two are hypermixer configurations (ramp and alternating-wedge). All three pylons exhibit the same frontal area to the airflow. A cold-flow CFD simulation with ethylene fuel injection and cold-flow wind-tunnel experiments (using aerothermal probe, Raman spectroscopy, and NO-PLIF experimental techniques) with air and methane injection are accomplished for each pylon.

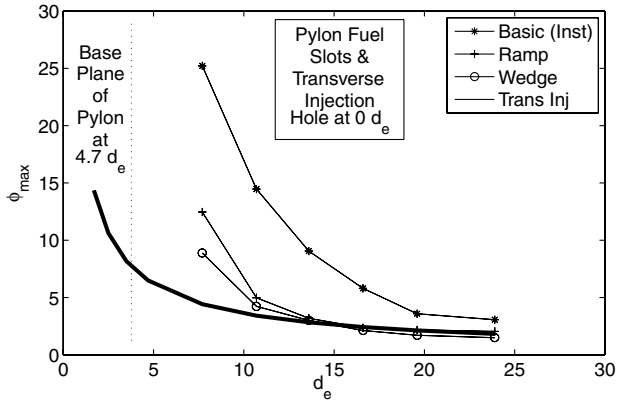

Fig. 30 Plume-dilution comparison between pylons and transverse injection.

In simulations, the ramp and alternating-wedge pylons (hypermixer pylons) show decisive near-field increases in streamwise vortical motion compared with the basic pylon. This increase in streamwise vortical motion results in better mixing for those pylons, bringing a larger area of fuel/air mixture to flammable conditions in a shorter distance. This is verified by both simulation data and data from the Raman and NO-PLIF experiments. The mixing enhancement of the hypermixer pylons moves the combustible mixture region closer to the base plane of the pylon compared with the basic pylon. In practice, this could result in shorter required combustor lengths. In addition, a combustion flame closer to the pylon base plane, where velocities are smaller in magnitude, is advantageous for the pylon's use as a flameholder. Between the hypermixer pylons, the alternating-wedge has a slight mixing advantage over the ramp pylon.

There is a measurable increase in total pressure loss accompanying the increased mixing effectiveness in the case of the alternating-wedge pylon compared with the basic pylon. The ramp pylon total-pressure-loss increase compared with the basic pylon, if present, appears to be negligible. The ramp and basic pylons are very close in total pressure loss. These results are verified by both simulation data and data from the aerothermal probe experiments. In addition, from simulation data, it is observed that the alternating-wedge pylon exhibits the highest drag, the basic pylon has the second highest, and the ramp pylon has the lowest drag. The ramp and basic pylons are very close in drag values.

The question is how one trades off an increase in mixing performance versus an increase in total pressure loss to the airflow. At first glance, the results could justify the ramp pylon as the best overall performer. It provides an increased mixing capability over the basic pylon while maintaining a total pressure loss very close to the basic pylon. On the other hand, the increased mixing effectiveness of the alternating-wedge pylon over the ramp pylon could offset the slight increase in total pressure loss. Because all experiments conducted here are cold flow, it is impossible to answer the question definitively for a combustor flow. A combustion simulation or experiment needs to be accomplished to answer this tradeoff question.

A few comparisons between simulation and experimental results were made. One qualitative comparison was between plume-dilution measurements from simulation and NO-PLIF experiments, because the injectant gases were very similar in molecular weight (ethylene vs air) and the test conditions were comparable. Very similar trends are observed in the normalized concentration measures. The alternating-wedge pylon dilutes the plume the fastest, followed closely by the ramp pylon, and then the basic pylon. In addition, there are similar injectant decay rates with downstream distance and similar differences between instantaneous and averaged concentration measures in the case of the basic pylon.

In another comparison, ethylene plume-dilution measurements from simulation of the three pylons were directly compared with ethylene plume-dilution measurements from experimental investigation of a transverse circular wall injector studied in past research. If compared from the point of fuel injection (pylon fueling slots), the hypermixer pylon plumes equal the mixed state of the transverse wall

injector plume around 65 mm downstream of the pylon base plane. If the transverse wall injector were placed at the position of the pylon base plane, the mixed state of the hypermixer pylon plumes would equal the transverse wall injector plume everywhere. This shows hypermixer geometries placed on an in-stream pylon can greatly improve mixing performance, rivaling the mixing capability of a transverse wall injector.

Acknowledgment

The views expressed in this paper are those of the authors and do not reflect the official policy or position of the U.S. Air Force, U.S. Department of Defense, or the U.S. Government.

References

[1] Smart, M., and Trexler, C., "Mach 4 Performance of Hypersonic Inlet with Rectangular-to-Elliptical Shape Transition," *Journal of Propulsion and Power*, Vol. 20, No. 2, Mar.–Apr. 2004, pp. 288–293. doi:10.2514/1.1296

[2] Bulman, M., and Siebenhaar, A., "The Rebirth of Round Hypersonic Propulsion," AIAA Paper 2006-5035, 2006.

[3] Tam, C., Lin, K., and Raffoul, C., "Review of Jet-in-Crossflow Studies for Scramjet Application," U.S. Air Force Research Lab., Wright–Patterson AFB, OH, 2007.

[4] Tam, C., Hsu, K., Gruber, M., and Raffoul, C., "Aerodynamic Performance of an Injector Strut for a Round Scramjet Combustor," AIAA Paper 2007-5403, 2007.

[5] Doster, J., King, P., Gruber, M., and Maple, R., "Pylon Fuel Injector Design for a Scramjet Combustor," AIAA Paper 2007-5404, 2007.

[6] Kirchhartz, R., Mee, D., and Stalker, R., "Skin Friction Drag with Boundary Layer Combustion in a Circular Combustor," AIAA Paper 2008-2589, 2008.

[7] Gruber, M., Nejad, A., Chen, T., and Dutton, J., "Transverse Injection from Circular and Elliptical Nozzles into a Supersonic Crossflow," *Journal of Propulsion and Power*, Vol. 16, No. 3, May–Jun. 2000, pp. 449–457. doi:10.2514/2.5609

[8] Kobayashi, K., Bowersox, R., Srinivasan, R., Carter, C., and Hsu, K., "Flowfield Studies of a Diamond-Shaped Fuel Injector in a Supersonic Flow," *Journal of Propulsion and Power*, Vol. 23, No. 6, Nov.–Dec. 2007, pp. 1168–1176. doi:10.2514/1.30000

[9] Gruber, M., Carter, C., Montes, D., Haubelt, L., King, P., and Hsu, K., "Experimental Studies of Pylon-Aided Fuel Injection into a Supersonic Crossflow," *Journal of Propulsion and Power*, Vol. 24, No. 3, May–Jun. 2008, pp. 460–470. doi:10.2514/1.32231

[10] Heiser, W., and Pratt, D., *Hypersonic Airbreathing Propulsion*, AIAA Education Series, AIAA, Washington, D.C., 1994.

[11] Curran, E., and Murthy, S., *Scramjet Propulsion, of Progress in Astronautics and Aeronautics*, Vol. 189, AIAA, Reston, VA, 2000.

[12] Aria, T., Sakaue, S., Morisaki, T., Kondo, A., Hiejima, T., and Nishioka, M., "Supersonic Streamwise Vortices Breakdown in a Scramjet Combustor," AIAA Paper 2006-8025, Nov. 2006.

[13] Northam, G., Greenberg, I., Byington, C., and Capriotti, D., "Evaluation of Parallel Injector Configurations for Mach 2 Combustion," *Journal of Propulsion and Power*, Vol. 8, No. 2, Mar.–Apr. 1992, pp. 491–499. doi:10.2514/3.23503

[14] Riggins, D., and, Vitt, P., "Vortex Generation and Mixing in Three-Dimensional Supersonic Combustors," *Journal of Propulsion and Power*, Vol. 11, No. 3, May–Jun. 1995, pp. 419–426. doi:10.2514/3.23860

[15] Abdel-Salam, T., Tiwari, S., and Mohieldin, T., "Effects of Ramp Side Angle in Supersonic Mixing," *AIAA Journal*, Vol. 41, No. 6, Jun. 2003, pp. 1199–1201. doi:10.2514/2.2064

[16] Kawano, S., Aso, S., and Orino, M., "A Study of a New Injector for Improvement of Supersonic Mixing," AIAA Paper 2000-0089, Jan. 2000.

[17] Shreenivasan, O., Kumar, R., Kumar, T., Sujith, R., and Chakravarthy, S., "Mixing in Confined Supersonic Flow Past Strut Based Cavity and Ramps," AIAA Paper 2004-4194, July 2004.

[18] Manoharan, S., Chandra, B., Chakravarthy, S., Ramakrishnan, S., and Subramanyam, J., "Experimental Studies of Supersonic Cold Flow Mixing with Ramp Mixers," *Journal of Aerospace Engineering*, Vol. 18, No. 4, Oct. 2005, pp. 197–205. doi:10.1061/(ASCE)0893-1321(2005)18:4(197)

[19] Sunami, T., Wendt, M., and Nishioka, M., "Supersonic Mixing and Combustion Control Using Stream-Wise Vortices," AIAA Paper 1998-3271, July 1998.

[20] Sunami, T., and Scheel, F., "Analysis of Mixing Enhancement Using Streamwise Vortices in a Supersonic Combustor by Application of Laser Diagnostics," AIAA Paper 2002-5203, Oct. 2002.

[21] Sunami, T., Magre, P., Bresson, A., Grisch, F., Orain, M., and Kodera, M., "Experimental Study of Strut Injectors in a Supersonic Combustor Using OH-PLIF," AIAA Paper 2005-3304, May 2005.

[22] Mao, M., Riggins, D., and McClinton, C., "Numerical Simulation of Transverse Fuel Injection," NASA Langley Research Center, TR N91-21097, Hampton, VA, 1991.

[23] Fuller, R., Wu, P., Nejad, A., and Schetz, J., "Comparison of Physical and Aerodynamic Ramps as Fuel Injectors in Supersonic Flow," *Journal of Propulsion and Power*, Vol. 14, No. 2, Mar.–Apr. 1998, pp. 135–145. doi:10.2514/2.5278

[24] Glassman, I., *Combustion*, Academic Press, New York, 1996.

[25] Hsu, K., Carter, C., Crafton, J., Gruber, M., Donbar, J., and Mathur, T., "Fuel Distribution About a Cavity Flameholder in Supersonic Flow," AIAA Paper 2000-3585, 2000.

[26] Gruber, M., Donbar, J., Carter, C., and Hsu, K., "Mixing and Combustion Studies Using Cavity-Based Flameholders in a Supersonic Flow," *Journal of Propulsion and Power*, Vol. 20, No. 5, Sept.–Oct. 2004, pp. 769–778. doi:10.2514/1.5360

[27] Murugappan, S., Gutmark, E., Carter, C., Donbar, J., Gruber, M., and Hsu, K., "Transverse Supersonic Controlled Swirling Jet in a Supersonic Cross Stream," *AIAA Journal*, Vol. 44, No. 2, Feb. 2006, pp. 290–300. doi:10.2514/1.13312

[28] Gruber, M., and Nejad, A., "New Supersonic Combustion Research Facility," *Journal of Propulsion and Power*, Vol. 11, No. 5, 1995, pp. 1080–1083. doi:10.2514/3.23940

[29] Eckbreth, A., *Laser Diagnostics for Combustion Temperature and Species*, Abacus, Preston, England, U.K., 1988.

[30] Demtroder, W., *Laser Spectroscopy*, Springer, New York, 2003.

[31] Kinney, J., *Statistics for Science and Engineering*, Addison Wesley, Reading, MA, 2002.

[32] Haubelt, L., King, P., Gruber, M., Carter, C., and Hsu, K., "Performance of Pylons Upstream of a Cavity-Based Flameholder in Non-Reacting Supersonic Flow," AIAA Paper 2006-4679, July 2006.

C. Segal
Associate Editor